#### Contents lists available at ScienceDirect

# Petroleum Science

journal homepage: www.keaipublishing.com/en/journals/petroleum-science



# **Original Paper**

# Mechanisms of organic matter accumulation in marine clear water conditions: The Upper Permian Dalong Formation, Sichuan Basin, China



Guo-Dong Xia <sup>a, b</sup>, Yue-Hao Ye <sup>a, b, \*</sup>, Shu-Gen Liu <sup>a, d</sup>, Hua Wang <sup>c</sup>, Kun Jiao <sup>a, b</sup>, Jin-Min Song <sup>a, b</sup>, Zhi-Wu Li <sup>a</sup>, Wei Chen <sup>a</sup>, Ying Ming <sup>c</sup>, Xiao-Gang Ma <sup>a</sup>, Heng Wang <sup>a, b</sup>, Chun-Qiao Yan <sup>a, b</sup>, Yun Zeng <sup>e</sup>

- a State Key Laboratory of Oil and Gas Reservoir Geology and Exploitation, Chengdu University of Technology, Chengdu, 610059, Sichuan, China
- <sup>b</sup> College of Energy, Chengdu University of Technology, Chengdu, 610059, Sichuan, China
- <sup>c</sup> Exploration and Development Research Institute, PetroChina Southwest Oil and Gasfield Company, Chengdu, 610041, Sichuan, China
- <sup>d</sup> Xihua University, Chengdu, 610039, Sichuan, China
- <sup>e</sup> Department of International Education, Yibin University, Yibin, 644000, Sichuan, China

#### ARTICLE INFO

#### Article history: Received 29 May 2024 Received in revised form 5 January 2025 Accepted 21 March 2025 Available online 24 March 2025

Edited by Jie Hao

Keywords: Ultrahigh Intra-cratonic sag Well DY-1H Benthic plants II2 kerogen Restricted

#### ABSTRACT

The Late Permian to Early Triassic marked a pivotal phase in paleoenvironmental and tectonic shifts. The Kaijiang-Liangping intracratonic sag, a tectonic geomorphology formed by Emei taphrogenesis in the Sichuan Basin, is situated within a clear water carbonate platform. Under these conditions, the black shales of the Dalong Formation in the sag have ultrahigh organic matter content. However, the mechanism by which these conditions control the accumulation of such organic matter remains unclear. Petrological and geochemical analyses of well DY-1H revealed four distinct units within the Dalong Formation: A, B, C, and D, with average total organic carbon contents of 3.00%, 9.59%, 4.57%, and 0.27%, respectively. The kerogen maceral, carbon isotope, and pyrolysis results show that the organic matter mainly comprises Type II<sub>2</sub> kerogen. Benthic plants growing in clear water may be the primary source of this kerogen. Shallow water, suboxic conditions, strong volcanism, and high productivity characterize Unit A. Unit B features restricted ocean circulation, anoxic conditions, weak upwelling, moderate volcanism, and high productivity. Unit C is characterized by anoxic conditions, strong upwelling, weak volcanism, and moderate productivity. Oxic conditions and low productivity define Unit D. These findings challenge traditional models that struggle to explain the accumulation of ultrahigh organic matter in Unit A under suboxic conditions, Unit C under moderate productivity, and Unit B with abnormally high organic matter content. The flourishing of benthic plants, a considerable source of Type II<sub>2</sub> kerogen that resists decomposition and favors preservation, is the dominant factor controlling the ultrahigh organic matter accumulation of black shales in Units A, B, and C under clear water conditions. Oxidized bottom waters and decreased benthic plant growth were crucial to the sharp decline in organic matter.

© 2025 The Authors. Publishing services by Elsevier B.V. on behalf of KeAi Communications Co. Ltd. This is an open access article under the CC BY license (http://creativecommons.org/licenses/by/4.0/).

#### 1. Introduction

Organic-rich deposits have long intrigued geologists owing to their widespread distribution at specific periods and their early recognition as potential oil-prone source rocks (Sageman et al., 2003). Two models are commonly used to explain organic matter accumulation: the "productivity model" and the "preservation

\* Corresponding author. E-mail address: bestone86@163.com (Y.-H. Ye).

model" (Demaison and Moore, 1980; Tyson and Pearson, 1991; Sageman et al., 2003).

The Late Permian, marking the end of the Paleozoic, represents a critical interval in Earth's history characterized by global environmental and biological changes (Farabegoli et al., 2007; Song et al., 2015). These include the convergence of Pangea (Muttoni et al., 2003), superplumes and volcanism (Cocks and Torsvik, 2007), ocean acidification and toxicity, global hypoxia, climate change (Huey and Ward, 2005), widespread deposition of black shales (Shen et al., 2015), and subsequent mass extinction (Wignall and

Twitchett, 1996). The Sichuan Basin, located in the eastern Paleo-Tethys region of the multi-island—oceanic system (Yu et al., 2021), formed the Kaijiang-Liangping intracratonic sag (K-L intracratonic sag; Fig. 1) under the influence of Emei taphrogenesis during the Late Permian (Liu et al., 2021b). Many wells and outcrops indicate that the black shale of the Dalong Formation in the intracratonic sag has high organic matter content.

Sedimentation can be divided into "turbid" and "clear" waters (Wang, 1988; Nichols, 2023). As early as 1965, the famous sedimentologist M. L. Irwin published the paper "General theory of epeiric clear water sedimentation" in the AAPG Bulletin and first put forward the term "clear water." Clear-water sedimentation refers to processes that ideally produce sediments in epeiric marine waters that have received no influx of terrigenous clastics (Irwin, 1965). Traditionally, the widely studied shales with high organic matter, especially the Paleozoic-Mesozoic shales (including the Cambrian Qiongzhusi shale, the Ordovician-Silurian Wufeng-Longmaxi shale, and the Devonian Marcellus shale), have detrital clay minerals averaging over 35%, with some even as high as 60% (Chen et al., 2019; Wu et al., 2020; Yan et al., 2021), indicating typical turbid water conditions. However, the black shale of the Dalong Formation in the Sichuan Basin was deposited in the K-L intracratonic sag in the epeiric sea carbonate platform and surrounded by the homochronous Changxing Formation limestone (Fig. 1) with extremely low terrigenous input, indicating typical clear water conditions. Whether these clear water conditions stimulate ultrahigh organic matter accumulation is an issue that should be discussed in future studies. Hence, we attempt to answer this question by deciphering the mechanism of organic matter accumulation in the black shale of the Upper Permian Dalong in the northern Sichuan Basin.

In this study, we present detailed petrological and geochemical analyses of well DY-1H in the K-L intracratonic sag to establish the mechanism of ultrahigh organic matter accumulation in the Dalong Formation under clear water conditions and to provide new insights into global black shale organic matter accumulation.

#### 2. Geological setting

Most global plates converged in the Late Paleozoic, peaking in the Late Permian and forming Pangea (Fig. 1(a)) (Muttoni et al., 2003). The South China Plate was an independent block in the Late Permian, formed by the collision of the Yangtze Plate and the Cathaysian Plate (Fig. 1(b)), and was located in the equatorial warm water province on the eastern margin of the Paleo-Tethys Ocean, east of Pangaea (Fig. 1(a)) (Zhang et al., 2018).

The Late Permian was a crucial phase in the formation and evolution of the Sichuan Basin (Liu et al., 2021b). The Sichuan Basin, located on the northwestern margin of the Yangtze Platform, witnessed a series of pivotal tectonic events, such as the Paleo-Tethys Ocean expansion, Emeishan Large Igneous Province eruption, basement fault reactivation (Luo et al., 2004; Liu et al., 2021b; Yu et al., 2021), and Emei taphrogenesis (Liu et al., 2021b). The Emeishan Large Igneous Province eruption in the late Guadalupian period induced lateral extension of the upper crust, resulting in strong tectonic-sedimentary differentiation that shaped the tectonic pattern of the Sichuan Basin (Liu et al., 2021b). The K-L intracratonic sag developed in the northern Sichuan Basin (Fig. 1(c)) under the influence of Emei taphrogenesis, where the organic-rich shale of the Dalong Formation was deposited (Liao et al., 2019; Liu et al., 2019). Laterally, there are successive carbonate platform, reef beach, slope, and deep-shelf facies (Fig. 1(c)).

The Dalong Formation mainly consists of black carbonaceous shale, siliceous shale, and limestone. Black shale with a total organic carbon (TOC) > 1% in the Dalong Formation has a thickness of 10–30 m (Liao et al., 2019; Liu et al., 2019). Many bioherm limestones have recently been discovered on both edges of the K-L intracratonic sag (Hao et al., 2008; Li et al., 2015), indicating a clearwater sedimentary environment that lacks terrigenous input. Therefore, the Dalong Formation in the K-L intracratonic sag provides a good research opportunity for studying the organic matter accumulation mechanism under clear water conditions. Well DY-1H, selected for this study, is located south of the K-L intracratonic sag and is connected to the western Hubei intracratonic sag to the southeast (Fig. 1(c)).

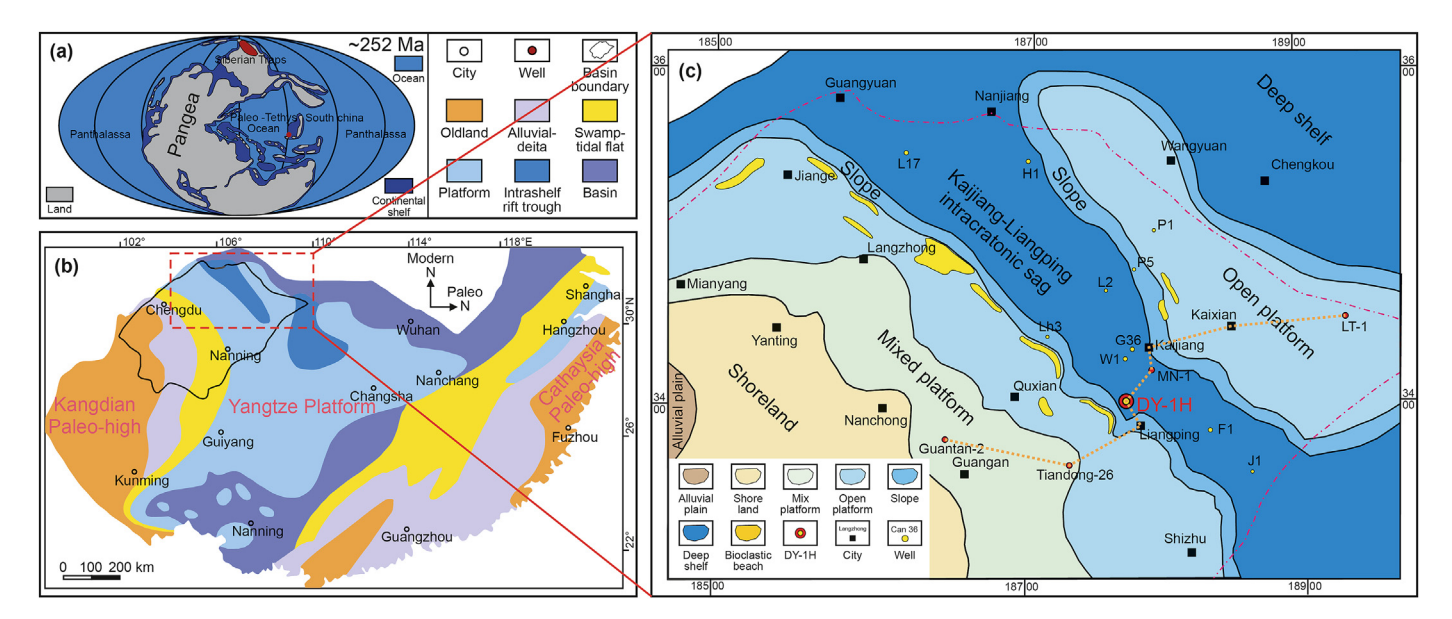


Fig. 1. (a) Global paleogeographic map of the Late Permian showcasing the location of South China, modified from Liu and Selby (2021). (b) Paleogeographic map of Late Permian South China showcasing the location of K-L intracratonic sag, modified from Yu et al. (2021). (c) Paleogeographic map of Late Permian in the northern margin of Sichuan Basin showcasing the location of well DY-1H.

#### 3. Lithofacies and sedimentary features

Well DY-1H is located in Longmen Village, approximately 17 km north of Liangping County in Chongqing City (Fig. 1(c)). The Dalong Formation conformably overlies the bioherm limestone of the Wuchiaping Formation. Based on its lithological assemblages, it can be vertically divided into four units (Units A. B. C. and D) (Fig. 2).

Unit A is a bioclast-bearing calcareous—siliceous mixed shale with a thickness of 2.10 m. The core of Unit A is mainly dark gray to black, with numerous bioclasts (Fig. 3(a) and (d); including small shelly fossils) observed in the core and thin sections. The bioclasts are mostly calcareous (Fig. 3(d)), with some silicified components (Fig. 3(d)). Interbedding of calcareous shale and thin limestone is observed at 4338.12 m (Fig. 3(b)). The most notable feature of Unit

A is the frequent occurrence of volcanic ash (Fig. 2). Three tuff layers occur in a core of approximately 2 m, with an average deposition of tuff every 0.67 m. The tuff thickness ranges from 10.31 to 50.53 mm, with an average of approximately 26.15 mm (Fig. 3(e) and (c)).

The lithology of Unit B is bioclast-bearing siliceous shale with a thickness of 7.30 m. Compared with Unit A, Unit B's color, lithology, and sedimentary and biological characteristics differ significantly. The siliceous shale of Unit B is darker and predominantly black. The most notable feature of Unit B is the decrease in calcareous bioclasts and the increase in fine authigenic silica (Fig. 3(f), (g), and (l)). Pyrite mainly occurs in thin layers (Fig. 3(i)), and a small amount of phosphorite is observed at the bottom (Fig. 3(h)). The frequency of tuff occurrence decreases, with three instances in the 7.3 m core. The average tuff deposition interval is 2.43 m (Fig. 2). The tuff

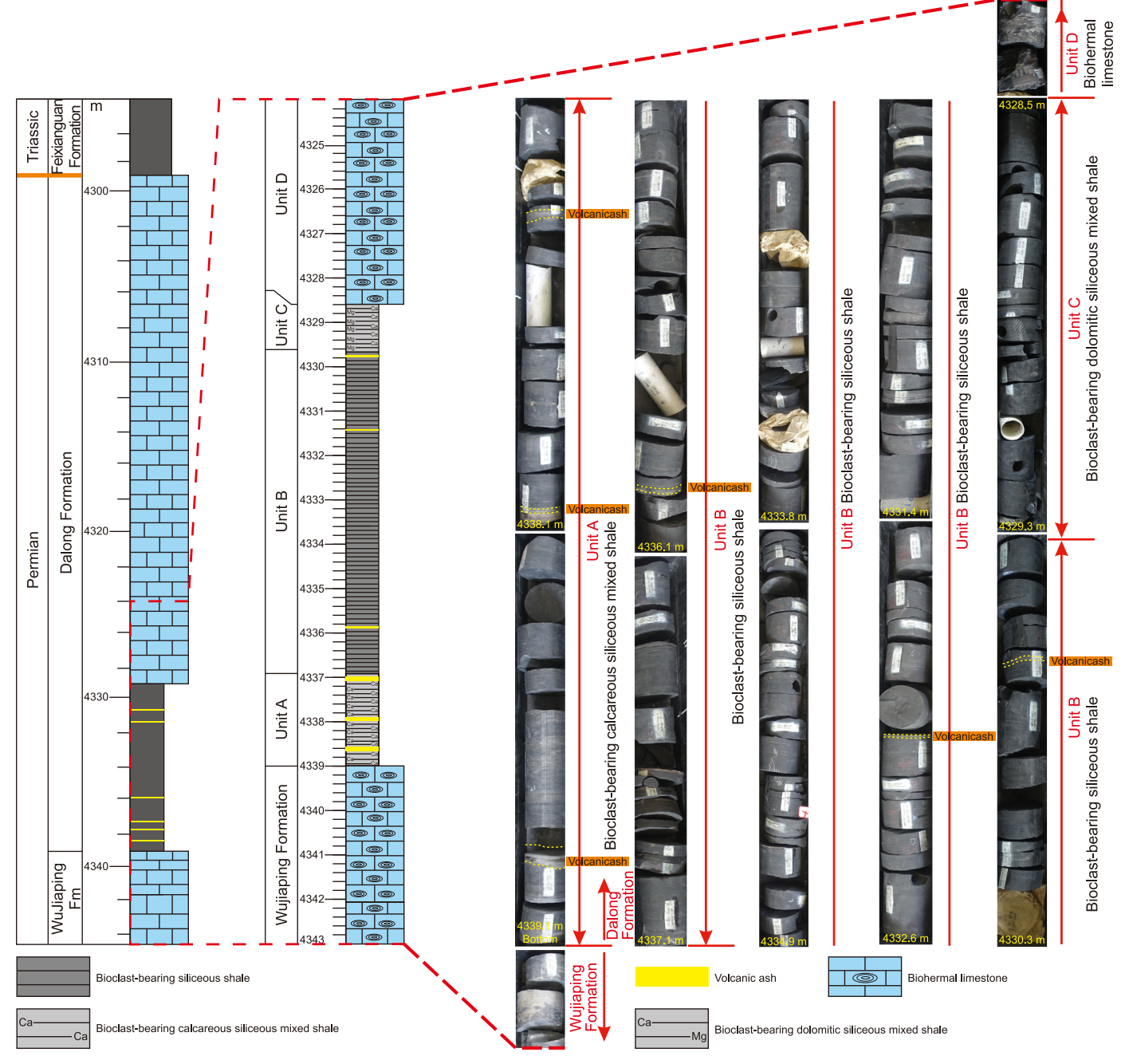
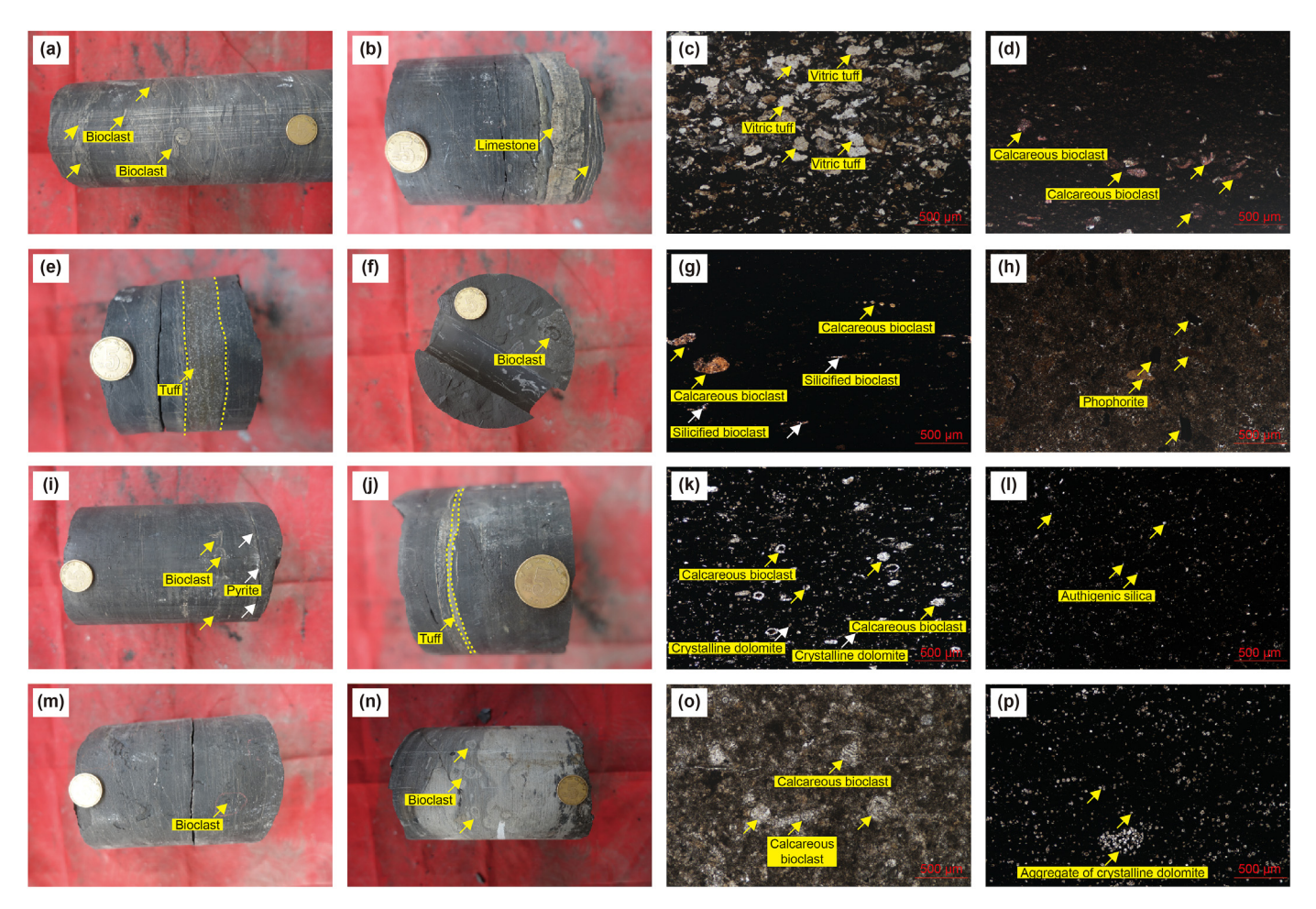


Fig. 2. Stratigraphic column and core photograph of the Dalong Formation in the well DY-1H, showing the thickness, lithofacies, and sedimentary features.



**Fig. 3.** Core and microscopic photographs of the lithologic and structural characteristics of the Dalong Formation in well DY-1H: (a) deep gray-black bioclast-bearing calcareous-siliceous mixed shale (depth of 4338.65 m); (b) interbedding of calcareous shale and thin limestone (depth of 4338.12 m); (c) rhyolitic—vitric tuff, the vitric tuff show subrounded-subangular shape, complete extinction under plane-polarized light, and undulatory extinction under cross-polarized light (depth of 4337.40 m); (d) bioclast-bearing calcareous siliceous mixed shale, the bioclasts are mostly calcite, some were silicified (white arrow) (sample DY-1H-1, depth of 4338.82 m); (e) gray-green tuff, approximately 17.6 mm thick (depth of 4337.40 m); (f) gastropod fossil in bioclast-bearing siliceous shale (depth of 4332.17 m); (g) a small amount of calcareous bioclasts in bioclast-bearing siliceous shale and authigenic silica can be observed (sample DY-1H-10, depth of 4336.61 m); (h) bioclast-bearing phosphorite, the phosphorus grains are mostly rounded or subrounded, indicating an endogenous sedimentation (depth of 4335.53 m); (i) bioclast-bearing siliceous shale, a vast of shelly fossils can be seen in the cores (yellow arrow) (depth of 4332.50 m); (j) gray-green tuff, approximately 6.62 mm thick (depth of 4337.40 m); (k) bioclast-bearing dolomitic—siliceous mixed shale, some calcareous bioclasts (yellow arrow) and crystalline dolomites (white arrow) can be observed (sample DY-1H-18, depth of 4329.25 m); (l) bioclast-bearing dolomitic—siliceous mixed shale (depth of 4328.70 m); (n-o) bioclast-bearing dolomitic—siliceous mixed shale (depth of 4328.70 m); (n-o) bioclast-bearing dolomitic—siliceous mixed shale (depth of 4328.70 m); (n-o) bioclast-bearing dolomitic—siliceous mixed shale (depth of 4328.70 m); (n-o) bioclast-bearing dolomitic—siliceous mixed shale (depth of 4328.70 m); (n-o) bioclast-bearing dolomitic—siliceous mixed shale (depth of 4328.70 m); (n-o) bioclast-bearing dolomitic—siliceous mixed shale (depth of 4328.70 m); (

thickness ranges from 6.62 to 12.91 mm, with an average of approximately 9.15 mm (Fig. 3(j)).

Unit C is bioclast-bearing dolomitic—siliceous mixed shale with a thickness of 0.98 m. The core of Unit C is mainly dark gray to black, with a large number of bioclasts (including small shelly fossils) observed in the core and thin sections (Fig. 3(m)). The most significant feature of Unit C is the increase in dolomite content (Fig. 3(k) and (p)); a large number of idiomorphic fine crystalline dolomites occur in the thin section (Fig. 3(k) and (p)). Argillaceous fine-grained dolomite is present at the top. Tuff is absent in Unit C (Fig. 2).

The lithology of Unit D is bioclastic limestone with a thickness of 30.20 m (Fig. 1(d)). The Dalong Formation of Unit D transitions from black shale to grayish-white bioclastic limestone. Large numbers of bioclasts are observed in the cores and thin sections (Fig. 3(m) and (o)).

Finally, data from seven wells were obtained and correlated with DY-1H (Fig. 4). The stratigraphic correlation shows that the black shale in the lower part of the Dalong Formation diminishes

from the sag to both sides, and the mudstone in the upper part of the Dalong Formation gradually transitions into bioclastic limestone.

#### 4. Samples and analytical methods

Ten samples were collected for organic petrology analysis, and 19 samples were collected for whole-rock X-ray diffraction (XRD) analysis (Table 1). Twenty-four samples were collected from well DY-1H for thin-section analysis, TOC, major elements, and trace elements (Tables 2 and 3). In addition, one tuff sample and one phosphorite sample were collected for thin-section observations.

Organic petrological analyses (including kerogen and whole-rock maceral analyses) were conducted at the State Key Laboratory of Oil and Gas Reservoir Geology and Exploitation, Chengdu University of Technology, Chengdu, Sichuan, China. The sample was ground into a powder with a particle size of less than 100 mesh, followed by the Soxhlet extraction for kerogen maceral analysis. Diluted hydrochloric acid (5%) was added to the extract to remove

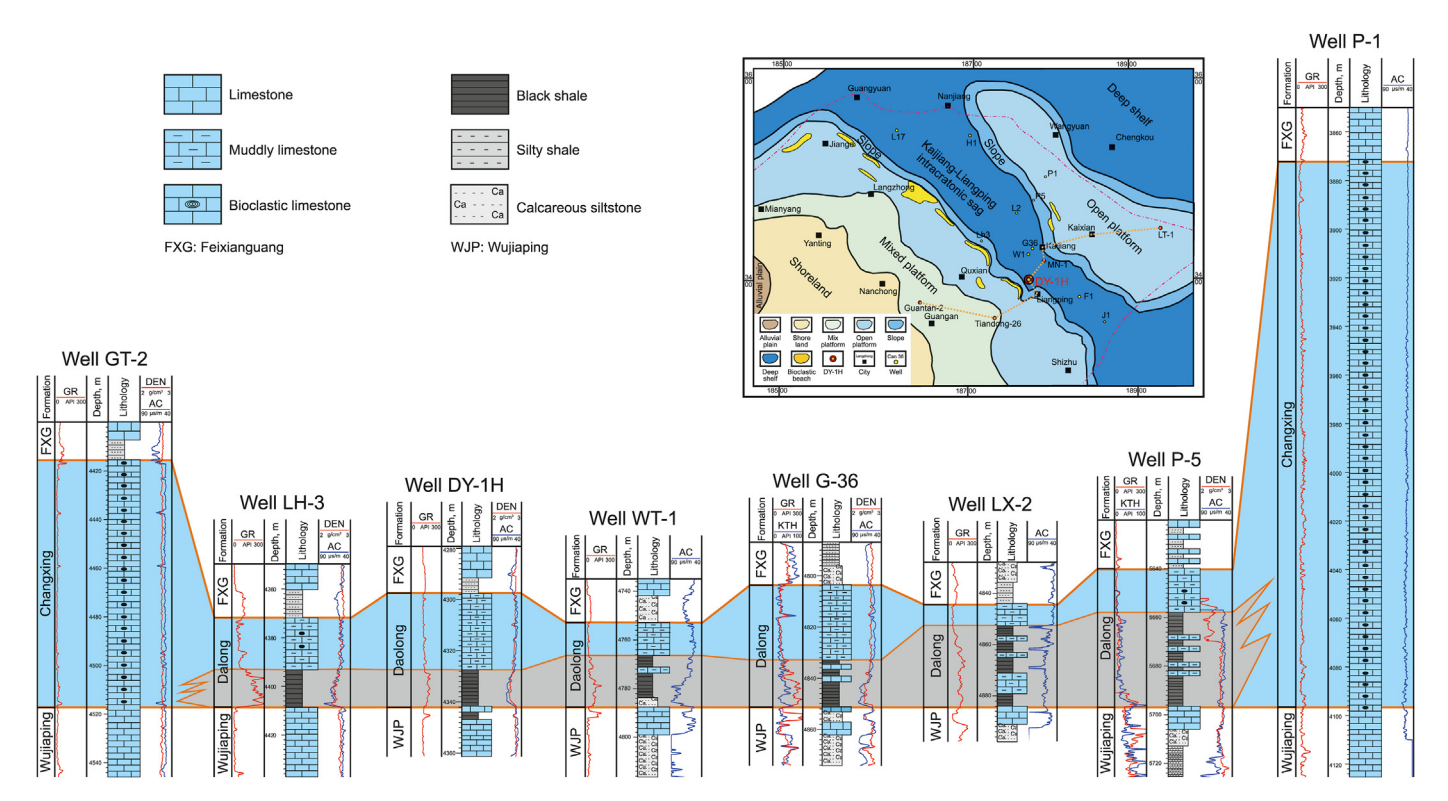


Fig. 4. Stratigraphic correlation of the well DY-1H with the wells GT-2, LH-3, WT-1, G-36, LX-2, P-5, and P-1.

**Table 1**Mineral composition and content of the Dalong Formation in the DY-1H well.

Samples	Depth, m	Quartz, %	Calcite, %	Dolomite, %	Clay, %	Feldspar, %	Siderite, %	Pyrite, %	Fluorapatite, %
DY-1H-19S	4325.95	17	81.9	0	0	0.7	0	0.4	0
DY-1H-18S	4326.64	3.9	86.6	0	7.1	2.4	0	0	0
DY-1H-17S	4327.10	6.4	50.9	40.8	0	1.9	0	0	0
DY-1H-16S	4328.60	30.8	42.1	4.9	9.7	7.4	0	5.1	0
DY-1H-15S	4329.25	65.2	20.4	3.3	0	5.5	0	5.7	0
DY-1H-14S	4330.52	60.1	16.3	0	11.8	7.5	0	4.3	0
DY-1H-13S	4330.57	45.1	37.3	0	6.6	6.1	0	4.9	0
DY-1H-12S	4330.98	47.2	39.2	1.4	0	7.4	0	4.7	0
DY-1H-11S	4334.09	64	17	1.9	8.7	4.7	0	3.7	0
DY-1H-10S	4334.30	58.5	21.1	1.4	8.4	5.4	0	5.3	0
DY-1H-9S	4334.57	72.1	6.8	1.3	6.6	6.8	3.5	2.8	0
DY-1H-8S	4334.72	61.9	11.9	3.9	14.5	4	0	3.8	0
DY-1H-7S	4334.94	67.8	12.8	0.9	7.1	4	3	4.4	0
DY-1H-6S	4335.48	60.9	13	1.7	14.3	6.1	0	3.9	0
DY-1H-5S	4336.17	57.2	18.7	2.7	6.7	7.4	4.3	3.1	0
DY-1H-4S	4336.70	55.6	5.7	1.8	15	4.3	0	6.6	11
DY-1H-3S	4337.20	32.7	45	1.6	14.2	6.5	0	0	0
DY-1H-2S	4337.40	9.3	13.8	0	67.3	4.1	0	5.4	0
DY-1H-1S	4338.20	17.2	59.2	3.1	10	3.8	0	4.5	2.2

the soluble organic matter. Subsequently, 5% diluted hydrochloric acid and hydrofluoric acid were added at a ratio of 1:2 to remove silicate minerals. Finally, 5% diluted hydrochloric acid was added to remove the newly formed salt minerals. After the aforementioned steps were repeated thrice, sodium hydroxide (0.5 M) was added to remove the alkali. Finally, pyrite and other minerals were removed by flotation in the centrifuge to obtain the separated/purified kerogen, which was then placed in an oven at 60 °C for drying. The kerogen was then cut into thin sections for optical microscopy. For whole-rock maceral analysis, the rock was sliced with a 5:1 mixture of Buehler epoxy resin and a curing agent, fixed on a slide, and polished. The polished glass slides were placed under a Nikon LHS2H100C21 optical microscope, and optical microscopy was performed under transmitted light and fluorescence.

XRD analysis was performed at the State Key Laboratory of Oil and Gas Reservoir Geology and Exploitation, Chengdu University of Technology, Chengdu, Sichuan, China. The mineral compositions were determined using XRD, and a detailed procedure was conducted following the China Petroleum Industry standard SY/T 5163—2018 (analysis method for clay minerals and ordinary nonclay minerals in sedimentary rocks by XRD). Computer analyses of the diffraction patterns revealed the relative abundances of various mineral phases, and a semi-quantitative assessment was performed.

Major and trace elements were tested at the Minerals Lab of ALS Chemex (Guangzhou) Co., Ltd., China. The major elements were analyzed using an X-ray fluorescence spectrometer (Philips PW2404). The analytical procedures followed the Chinese National

**Table 2**Major element concentrations of Dalong Formation's samples from the DY-1H well.

Samples	Depth, m	SiO <sub>2</sub> , %	Al <sub>2</sub> O <sub>3</sub> , %	CaO, %	Fe <sub>2</sub> O <sub>3</sub> , %	K <sub>2</sub> O, %	MgO, %	MnO <sub>2</sub> , %	Na <sub>2</sub> O, %	P <sub>2</sub> O <sub>5</sub> , %	SO <sub>2</sub> , %	TiO <sub>2</sub> , %	Loss on ignition, %
DY-1H-24	4324.00	37.88	0.67	30.29	0.54	0.16	0.78	0.02	0.18	0.04	0.09	0.07	28.73
DY-1H-23	4325.00	28.71	0.13	38.97	0.24	0.05	0.63	0.01	0.12	0.02	0.06	0.05	30.48
DY-1H-22	4326.00	9.56	0.42	46.63	0.22	0.08	1.26	0.02	0.19	0.05	0.12	0.07	41.29
DY-1H-21	4327.00	16.52	1.95	41.03	0.92	0.48	2.07	0.05	0.43	0.07	0.18	0.12	35.97
DY-1H-20	4328.60	58.49	5.43	12.91	1.60	1.11	0.98	0.02	0.90	0.52	0.06	0.17	16.97
DY-1H-19	4329.08	21.10	2.54	24.25	0.97	0.51	12.07	0.10	0.48	0.03	0.10	0.11	37.39
DY-1H-18	4329.25	51.54	4.74	12.91	4.24	1.02	2.62	0.04	0.60	0.06	0.17	0.25	20.47
DY-1H-17	4329.54	61.16	6.02	6.16	2.98	1.31	1.73	0.04	0.91	0.05	0.14	0.29	18.41
DY-1H-16	4330.06	63.22	3.88	10.98	1.62	0.92	0.73	0.03	0.53	0.06	0.20	0.16	16.88
DY-1H-15	4330.57	59.19	6.07	7.72	2.36	1.63	0.65	0.02	0.55	0.04	0.16	0.26	20.60
DY-1H-14	4331.42	45.69	12.36	8.78	4.04	2.95	1.51	0.05	1.43	0.10	0.13	0.61	21.65
DY-1H-13	4331.73	39.39	6.46	14.21	2.55	1.70	3.94	0.07	0.72	0.09	0.16	0.28	29.87
DY-1H-12	4332.17	43.24	5.65	18.66	2.45	1.62	0.79	0.03	0.62	0.21	0.08	0.27	25.39
DY-1H-11	4332.86	53.42	14.48	3.91	6.76	3.85	0.89	0.05	1.17	0.05	0.11	0.59	13.87
DY-1H-10	4333.61	46.03	6.66	13.38	3.00	1.40	1.16	0.07	1.19	0.07	0.16	0.25	25.79
DY-1H-9	4334.09	55.00	5.81	6.13	4.19	1.43	0.60	0.03	0.64	0.05	0.16	0.29	24.82
DY-1H-8	4334.72	66.98	8.41	3.86	3.03	2.14	1.16	0.05	0.81	0.05	0.13	0.39	12.32
DY-1H-7	4335.19	53.52	6.00	7.38	3.50	1.41	0.69	0.05	0.80	0.08	0.08	0.32	25.24
DY-1H-6	4335.95	61.41	7.70	5.82	3.28	1.87	0.83	0.13	0.80	0.91	0.09	0.34	16.12
DY-1H-5	4336.70	63.15	6.74	0.94	2.30	1.61	0.70	0.05	0.58	0.25	0.15	0.33	22.54
DY-1H-4	4337.25	47.23	6.46	15.09	2.38	1.60	1.84	1.52	0.63	0.21	0.20	0.27	21.95
DY-1H-3	4337.79	53.78	8.66	9.00	5.29	2.11	1.39	0.89	0.77	0.15	0.19	0.39	16.70
DY-1H-2	4338.20	45.17	9.99	11.85	4.17	2.57	1.28	0.87	0.73	0.23	0.15	0.55	21.90
DY-1H-1	4338.83	48.95	13.65	11.45	2.82	3.58	1.86	0.59	0.85	0.25	0.06	0.60	14.70

**Table 3**Trace element concentrations and TOC content of Dalong Formation's samples from the DY-1H well.

Samples	TOC, %	Depth, m	V, ppm	Cr, ppm	Co, ppm	Cu, ppm	Zn, ppm	Zr, ppm	Mo, ppm	Ba, ppm	Th, ppm	U, ppm
DY-1H-24	0.13	4324.00	10.59	13.30	4.16	20.25	56.12	6.99	0.31	206.44	1.66	2.59
DY-1H-23	0.24	4325.00	11.22	16.33	3.58	6.41	26.70	6.57	0.73	351.72	0.09	2.43
DY-1H-22	0.34	4326.00	7.07	9.47	0.54	3.86	7.39	3.90	2.67	283.34	1.12	2.97
DY-1H-21	0.36	4327.00	30.02	17.50	2.65	12.34	26.26	13.34	1.03	133.56	4.64	3.66
DY-1H-20	2.39	4328.60	432.98	138.13	10.04	52.45	63.59	43.59	16.05	115.81	5.13	24.32
DY-1H-19	2.08	4329.08	507.13	59.81	3.17	13.53	46.73	20.10	37.41	75.56	2.15	10.74
DY-1H-18	5.3	4329.25	1418.77	208.63	14.15	57.81	143.28	71.67	127.23	950.43	3.07	25.34
DY-1H-17	8.52	4329.54	1513.91	209.62	12.47	55.70	52.89	56.81	331.69	537.04	4.97	18.50
DY-1H-16	9.53	4330.06	280.23	133.69	10.16	67.49	65.14	33.90	7.35	189.66	2.77	10.09
DY-1H-15	12.1	4330.57	820.00	345.20	12.44	176.91	178.06	59.78	24.17	166.85	8.09	15.64
DY-1H-14	7.35	4331.42	1782.51	339.35	16.48	119.31	213.77	123.73	34.86	222.93	10.07	13.13
DY-1H-13	5.93	4331.73	1111.60	228.49	12.92	111.70	175.40	63.31	85.49	255.78	5.02	18.11
DY-1H-12	7.21	4332.17	1216.03	274.21	13.24	90.44	133.79	62.50	40.83	207.52	5.44	29.36
DY-1H-11	10.7	4332.86	1022.44	274.74	64.41	144.02	236.48	120.51	37.26	1013.91	39.40	9.01
DY-1H-10	8.11	4333.61	1014.63	348.85	14.29	120.46	170.77	62.07	57.36	211.82	13.88	13.40
DY-1H-9	7.23	4334.09	1237.91	504.41	25.03	180.73	224.57	67.89	58.24	144.16	4.79	9.51
DY-1H-8	6.74	4334.72	469.79	271.96	16.65	93.63	121.64	91.87	21.58	234.92	8.22	7.54
DY-1H-7	10.4	4335.19	1132.21	395.31	18.40	181.32	222.01	165.84	74.21	172.75	5.40	12.13
DY-1H-6	14	4335.95	456.45	282.82	20.29	144.28	248.93	88.78	17.46	244.51	6.53	25.26
DY-1H-5	15.8	4336.70	460.49	434.39	19.66	182.09	368.70	108.75	9.83	189.76	6.49	19.43
DY-1H-4	2.92	4337.25	264.72	116.36	13.92	85.66	183.92	202.81	15.72	159.41	5.47	9.01
DY-1H-3	2.84	4337.79	370.44	152.68	30.71	100.44	161.21	79.54	91.90	270.19	5.51	12.28
DY-1H-2	3.45	4338.20	394.57	219.96	26.57	154.24	288.88	113.78	10.16	215.43	9.09	13.24
DY-1H-1	2.76	4338.83	153.56	99.31	19.45	48.61	157.33	336.15	1.28	371.13	14.47	3.29

standard GB/T14506.28—2010. Trace and rare earth elements (REEs) were examined using an inductively coupled plasma mass spectrometer (ICP-MS X-Series, Thermo Fisher Scientific), and the analytical procedures followed Chinese National Standard GB/T14506.30—2010. Detailed experimental procedures for the XRD and major and trace element tests can be found following the well-established analytical procedures outlined by Xia et al. (2024) and Xiao et al. (2019).

## 5. Results

#### 5.1. TOC

As shown in Table 3, the TOC values of the Dalong Formation ranged from 0.13% to 15.80%, with an average of 6.10%. The TOC

values of Units A, B, C, and D ranged from 2.76% to 3.45% (average = 3.00%), 5.93%—15.80% (average = 9.59%), 2.08%—8.52% (average = 4.57%), and 0.13%—0.36% (average = 0.27%). Generally, sediments with TOC contents greater than 3.0% are considered ultrahigh organic matter deposits (Algeo and Ingall, 2007).

## 5.2. Kerogen maceral analysis

This study adopted the kerogen maceral identification and classification method (SY/T 5125–1996), which is the standard for the oil and natural gas industry in the People's Republic of China. The kerogen maceral analysis results for Units A, B, and C showed that the kerogen was mainly composed of exinite and vitrinite. The most abundant maceral was exinite (e.g., humic amorphogen), ranging from 73.00% to 76.00%, with an average of 74.67%. The

vitrinite content ranged from 22.00% to 25.00%, with an average of 23.33%. Inertinite had an average content of 2.00%. The type index ranged from 15.80 to 19.50, averaging 17.87, and indicating that the kerogen was classified as Type II<sub>2</sub>. The detailed results are presented in the Discussion section.

#### 5.3. Mineral compositions

The results of the whole-rock XRD are shown in Table 1 and Fig. 5. The main components of the Dalong Formation's black shale (Units A, B, and C) were quartz, calcite, dolomite, and small amounts of feldspar, clay, and pyrite. The main components of Unit D limestone were calcite, dolomite, and quartz (Fig. 5a). The average quartz, calcite, dolomite, and clay contents in Unit A were 24.95%, 52.10%, 2.35%, and 12.10%, respectively, in Unit B they were 59.13%, 18.16%, 1.55%, and 9.06%, respectively, in Unit C they were 48.00%, 31.25%, 4.10%, and 4.85%, respectively, and in Unit D they were 9.10%, 73.13%, 13.60%, and 2.37%, respectively (Fig. 5(b)). The average quartz, calcite, and clay contents in the tuff of Unit A (depth of 4337.40 m) were 9.30%, 13.80%, and 67.30%, respectively.

#### 5.4. Major elements

As shown in Table 2 and Fig. 6(a), the average contents of SiO<sub>2</sub>, CaO, MgO, Al<sub>2</sub>O<sub>3</sub>, and TiO<sub>2</sub> in Unit A were 48.78%, 11.85%, 1.59%, 9.69%, and 0.45%, respectively, in Unit B they were 54.19%, 8.48%, 1.14%, 7.52%, and 0.34%, respectively, in Unit C they were 48.07%, 14.06%, 4.35%, 4.68%, and 0.20%, respectively, and in Unit D they were 23.17%, 39.23%, 1.19%, 0.79%, and 0.08%, respectively. Other oxides, such as  $Fe_2O_3$ ,  $K_2O$ ,  $Na_2O$ ,  $MnO_2$ ,  $P_2O_5$ ,  $TiO_2$ , and  $SO_2$  had average contents of less than 5% in all units.

The enrichment factors (EFs) of the selected elements were calculated using Eq. (1):

$$Y_{EF} = (Y/Al)_{sample} / (Y/Al)_{PAAS}$$
 (1)

where Y represents the weight percentages of the selected element, and Al represents the weight percentages of aluminum, and the subscript PAAS denotes the Post-Archean Australian Shale standard (Nance and Taylor, 1976). EF > 1 indicates that Y is enriched; otherwise, it is depleted (Algeo and Tribovillard, 2009). The average EFs of Unit A were SiO<sub>2</sub> (EF = 1.63), CaO (EF = 19.63), MgO (EF = 1.52), and TiO<sub>2</sub> (EF = 0.87), those of Unit B were SiO<sub>2</sub> (EF = 2.45), CaO (EF = 19.66), MgO (EF = 1.41), and TiO<sub>2</sub> (EF = 0.85), those of Unit C were SiO<sub>2</sub> (EF = 3.02), CaO (EF = 56.89), MgO (EF = 12.37), and TiO<sub>2</sub> (EF = 0.82), and those of Unit D were SiO<sub>2</sub> (EF = 23.05), CaO (EF = 11,719.29), MgO (EF = 21.40), and TiO<sub>2</sub> (EF = 3.46). Compared with the Post-Archean Australian Shale, SiO<sub>2</sub>, Cao, MgO, MnO<sub>2</sub>, and P<sub>2</sub>O<sub>5</sub> were highly enriched, but the terrigenous element TiO<sub>2</sub> was depleted in all units (Fig. 6(a)).

#### 5.5. Trace elements

As shown in Table 3 and Fig. 6(b), the average EFs of Unit A were Ba (EF = 0.76), Cu (EF = 4.14), Zn (EF = 4.86), Th (EF = 1.12), U (EF = 6.67), and Mo (EF = 66.86), those of Unit B were Ba (EF = 1.00), Cu (EF = 7.42), Zn (EF = 6.18), Th (EF = 1.50), U (EF = 14.02), and Mo (EF = 108.69), those of Unit C were Ba (EF = 2.48), Cu (EF = 3.44), Zn (EF = 3.84), Th (EF = 1.06), U (EF = 26.09), and Mo (EF = 470.37), and those of Unit D were Ba (EF = 27.06), Cu (EF = 8.94), Zn (EF = 17.69), Th (EF = 2.64), U (EF = 47.67), and Mo (EF = 60.76). Compared with PAAS (McLennan, 2001), the redox-sensitive elements Mo, U, V, and nutrient elements Cu and Zn were highly enriched in all units (Fig. 6(b)).

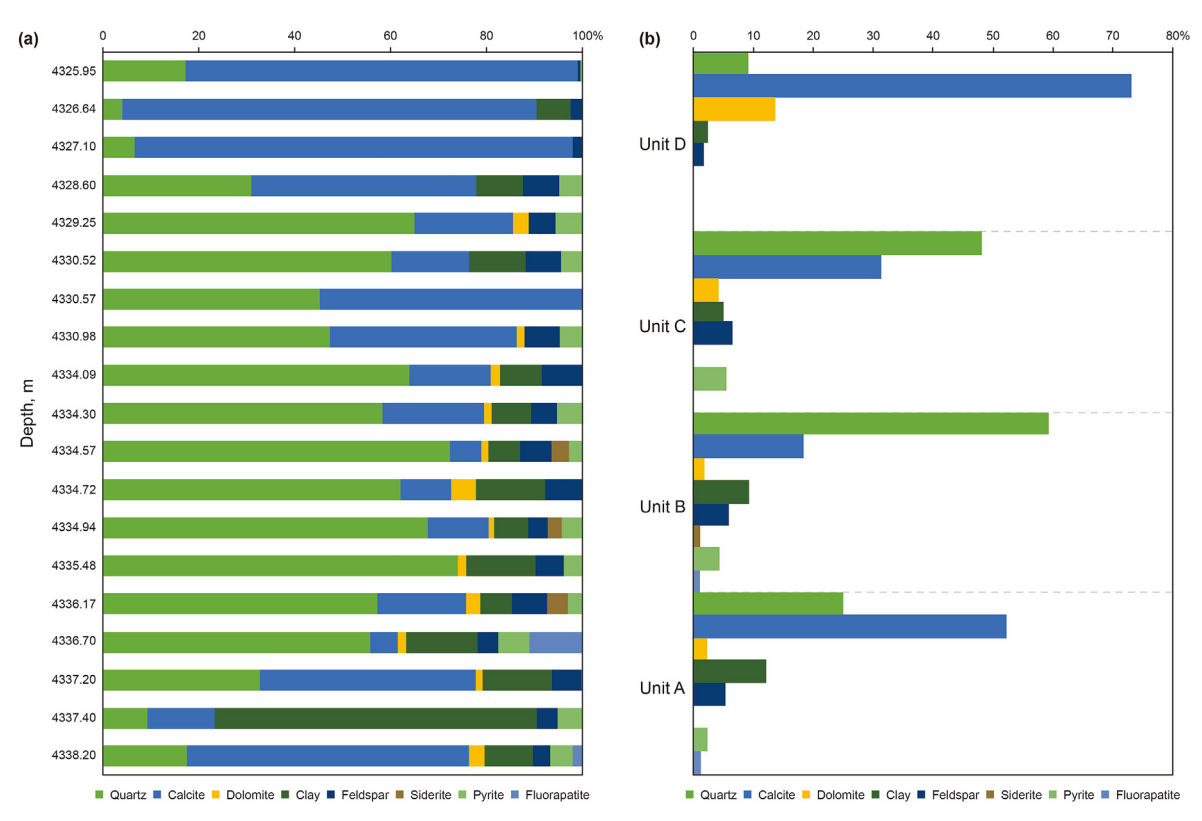


Fig. 5. (a) Percent stacked column diagram of the Dalong Formation's mineral compositions. (b) Mineral compositions of different units in the Dalong Formation.

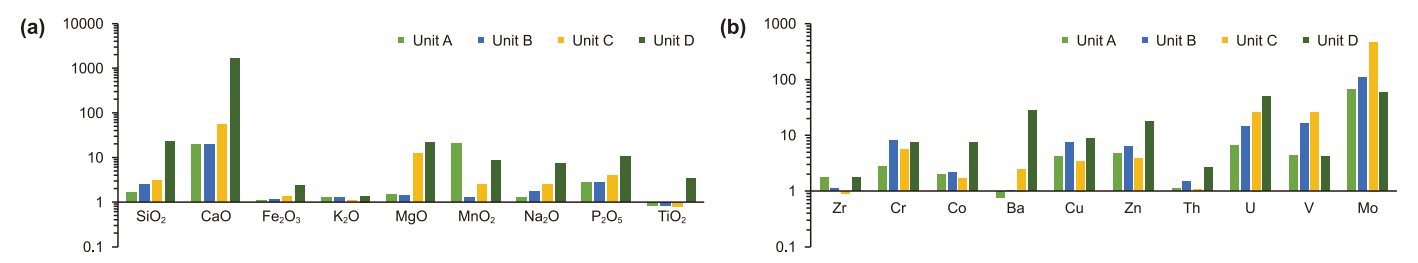


Fig. 6. (a) Major element enrichment factor (EF) of the Units A, B, C, and D (Mclennan, 2001). (b) Trace element enrichment factor (EF) of the units A, B, C, and D.

#### 6. Discussion

#### 6.1. Benthic plants may be the primary source of organic matter

The mechanism of organic matter accumulation in the Dalong Formation has been discussed in terms of tectonic setting and paleoenvironment (Wu et al., 2021, 2022; Yu et al., 2021; Lian et al., 2008; Liu et al., 2022a; Zheng et al., 2024). However, few studies have focused on the influence of organic matter type and source on organic matter accumulation. Studies have recognized that the high productivity associated with upwelling is the main driver of organic matter accumulation in the black shales of the Dalong Formation. However, to explain the source of this high productivity, in the absence of an analysis of the type and source of organic matter, the previous consensus was that plankton flourished (Wu et al., 2021; Yu et al., 2021; Liu et al., 2022b). Therefore, it is debatable whether plankton is responsible for this high productivity.

Although the latest classification scheme, from the International Committee for Coal and Organic Petrology 1994 completed the construction of the coal maceral classification system in 2017, a consensus regarding the maceral classification scheme for source rocks, especially Paleozoic source rocks, remains unresolved. The same terms often represent different meanings in the classifications of different authors (Sykorova et al., 2005; Ercegovac and Kostic, 2006). In this study, the maceral kerogen identification and type classification system (SY/T 5125–1996), the standard for China's oil and natural gas industry, was adopted. This system classified macerals into sapropelite, exinite, vitrinite, and inertinite. The kerogen and whole-rock maceral compositions of the analyzed black shales are illustrated in Fig. 7. Most shale samples from Units A, B, and C were dominated by exinite at approximately 74.67%. The exinite was predominantly humic amorphogen (Fig. 7(d), (e), and (f)). The second-highest content was vitrinite (approximately 23.33%; Fig. 7(a), (b), (c), (d), (e), and (f)). A small amount of inertinite, mainly fusinite (approximately 2%; Fig. 7(a), (b), (d), (e), and (f)), was observed. The kerogen and whole-rock maceral analyses show that the organic matter of the black shale of the Dalong Formation is rich in exinite and vitrinite and lean in sapropelite. The type index of the kerogen is Type II<sub>2</sub>. Rock pyrolysis and kerogen carbon isotope analyses have been performed on black shales of the Dalong Formation at the northern margin of the Sichuan Basin. The black shales of the Dalong Formation in the Changjiang Section, located in Guangyuan, have a HI index of 43.15 mg/g to 419.84 mg/g (average of 279.82 mg/g) and a  $T_{\text{max}}$  of 433–439 °C (average of 435 °C). The  $\delta^{13}$ C value of kerogen ranges from -28.4% to -25.2%, with an average value of -26.9%, and most samples range from -28.0% to -26.0%. The kerogen carbon isotopes and the cross-plot of HI and  $T_{\text{max}}$  show Type II<sub>2</sub> kerogen (Guo et al., 2023). Notably, two other well-known studies have confirmed these results (Hu et al., 2021; Fu et al., 2010).

Exinite (such as humic amorphogen) is different from sapropelites (such as sapropelic amorphogen), which are mainly formed

by the microbiological degradation of the epidermis and vascular tissue of plants (terrestrial or aquatic). Vitrinite is a maceral formed by the gelation of roots, stems, and bark and is composed of lignin and cellulose. The large amounts of exinite (such as humic amorphogen) and vitrinite observed in this study, strongly suggest that the organic matter in the black shale of the Dalong Formation was derived more from plants than from plankton. The clear-water environment was less affected by terrigenous inputs. Therefore, exinite (such as humic amorphogen) and vitrinite enriched in this environment, likely exclude the contribution of terrestrial plant inputs outside the basin. Lower benthic plants (including threadlike leaf plants and multicellular benthic macroalgae) have been observed in the Dalong Formation on the northern margin of the Sichuan Basin (Meng et al., 2008; Liang et al., 2009). Under weak extension and clear-water conditions, the sag with a moderate depth was almost within the photic zone. Optimal light conditions promoted the flourishing of lower benthic plants. These lower benthic plants likely provided large amounts of exinite (including humic amorphogen) and vitrinite. Compared to aliphatic compounds, aromatic compounds have stable structures and are not easily degraded (Carey and Sundberg, 2001; Höld et al., 1998). Sapropelite originates mainly from plankton, has a high H/C ratio, is rich in aliphatic compounds, and is prone to rapid bacterial decomposition. By contrast, exinite and vitrinite are mainly derived from plants, have a low H/C ratio, and are rich in aromatic compounds, making them difficult to decompose and exceptionally well-preserved. Therefore, the flourishing of benthic plants, which provided abundant exinite and vitrinite that are difficult to decompose and easy to preserve, may have been a critical cause of the ultrahigh organic matter accumulation in the Dalong Formation under clear-water conditions.

#### 6.2. Sedimentary records of volcanism and hydrothermal activity

### 6.2.1. Volcanism records

Volcanism is essential for biological evolution and environmental change (Elrick et al., 2017; Chapman et al., 2022; Dal Corso et al., 2022). Organic-rich deposits, such as the Upper Cretaceous Eagle Ford Formation and the Upper Ordovician Wufeng Formation-Lower Silurian Longmaxi Formation, are intrinsically related to volcanism (Wang et al., 2023). One hypothesis is that volcanic ash brings nutrients (such as Fe and P) to the water, causing a biological boom and enhancing productivity (Duggen et al., 2007; Lee et al., 2018; Liu et al., 2021a). In addition, volcanic ash brings many toxic and harmful substances (including Hg and Pb) to the sea, causing the death of organisms and inhibiting productivity (McKnight et al., 1981; Duggen et al., 2007). Soluble gases (such as H<sub>2</sub>S, SO<sub>2</sub>, and CO<sub>2</sub>) released by volcanic activity enter seawater (SW) in the form of acid rain, resulting in water stratification and bottom-water anoxia, which are conducive to the preservation of organic matter (Wignall, 2001; Shan et al., 2013; Li et al., 2021; Wang et al., 2023).

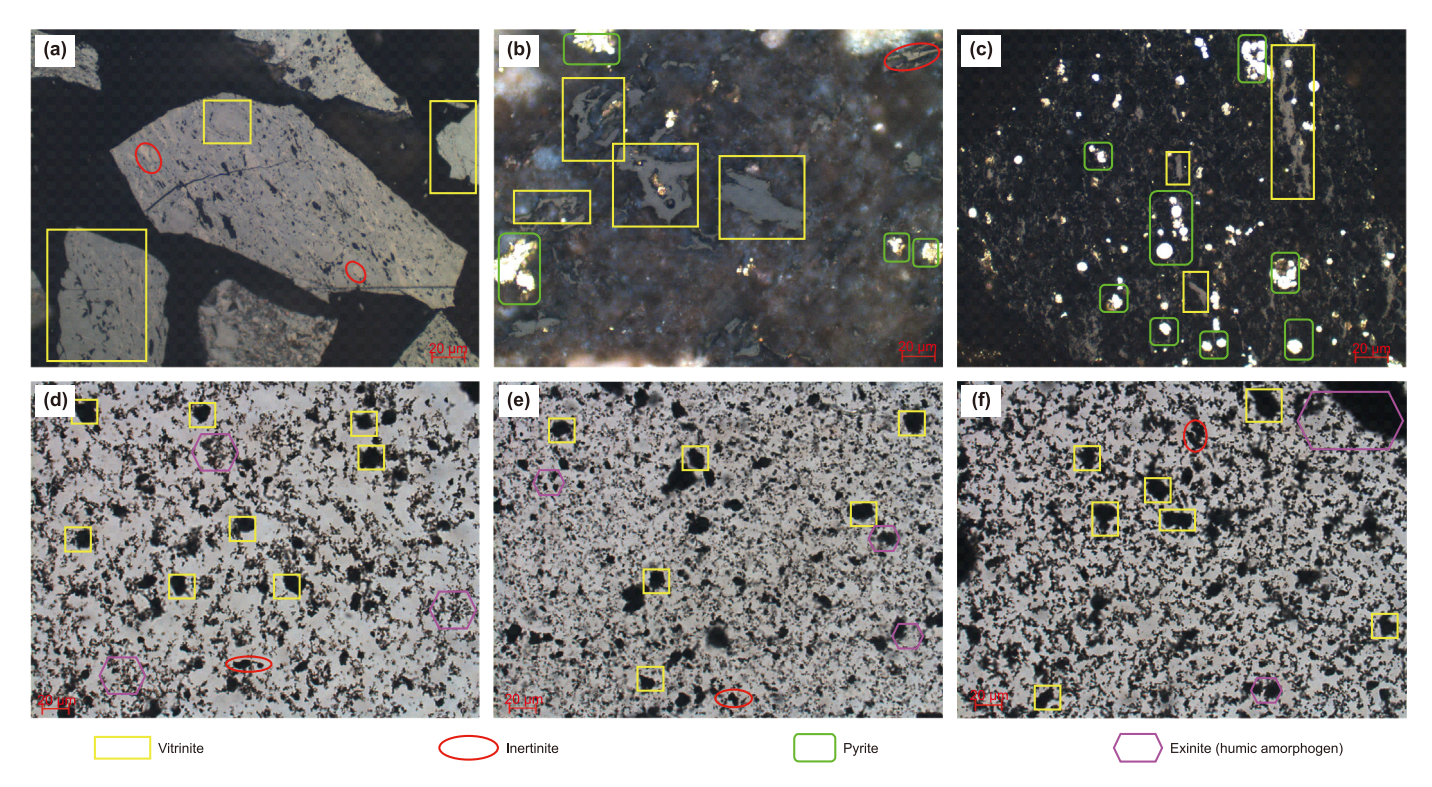


Fig. 7. Photomicrographs of whole rock and kerogen's macerals of the Dalong Formation's black shale in well DY-1H. (a) Whole rock macerals of sample DY-1H-9 (Unit A), (b) whole rock macerals of sample DY-1H-15 (Unit B), (c) whole rock macerals of sample DY-1H-24 (Unit C).

The volcanic ash layer provides direct evidence of volcanic activity. The intensity of the volcanic activity can be determined by the thickness and frequency of the ash layer (Du et al., 2021). In the core of well DY-1H, six layers of distinct tuff can be observed, showing a yellow-green color, which is easily distinguished from the black shales, with a continuous distribution and stable thickness. As described in "3. Lithofacies and Sedimentary Features" above Unit A, three tuff layers, each 2 m thick, were observed, with an average deposition of tuff every 0.67 m. The thickness of the tuff ranged from 10.31 to 50.53 mm, with an average of approximately 26.15 mm (Fig. 3(e) and (c)). The frequency of tuff occurrence decreased in Unit B, with the 7.3 m core containing three tuff layers. The average tuff deposition was every 2.43 m (Fig. 2). The thickness of the tuff ranged from 6.62 mm to 12.91 mm, with an average of approximately 9.15 mm (Fig. 3(j)). Tuff layers were absent in Units C and D (Fig. 2). Based on the thickness and frequency of the tuff in the core, it can be concluded that volcanism was strong in Unit A, moderate in Unit B, and began to weaken and eventually ceased in Unit C.

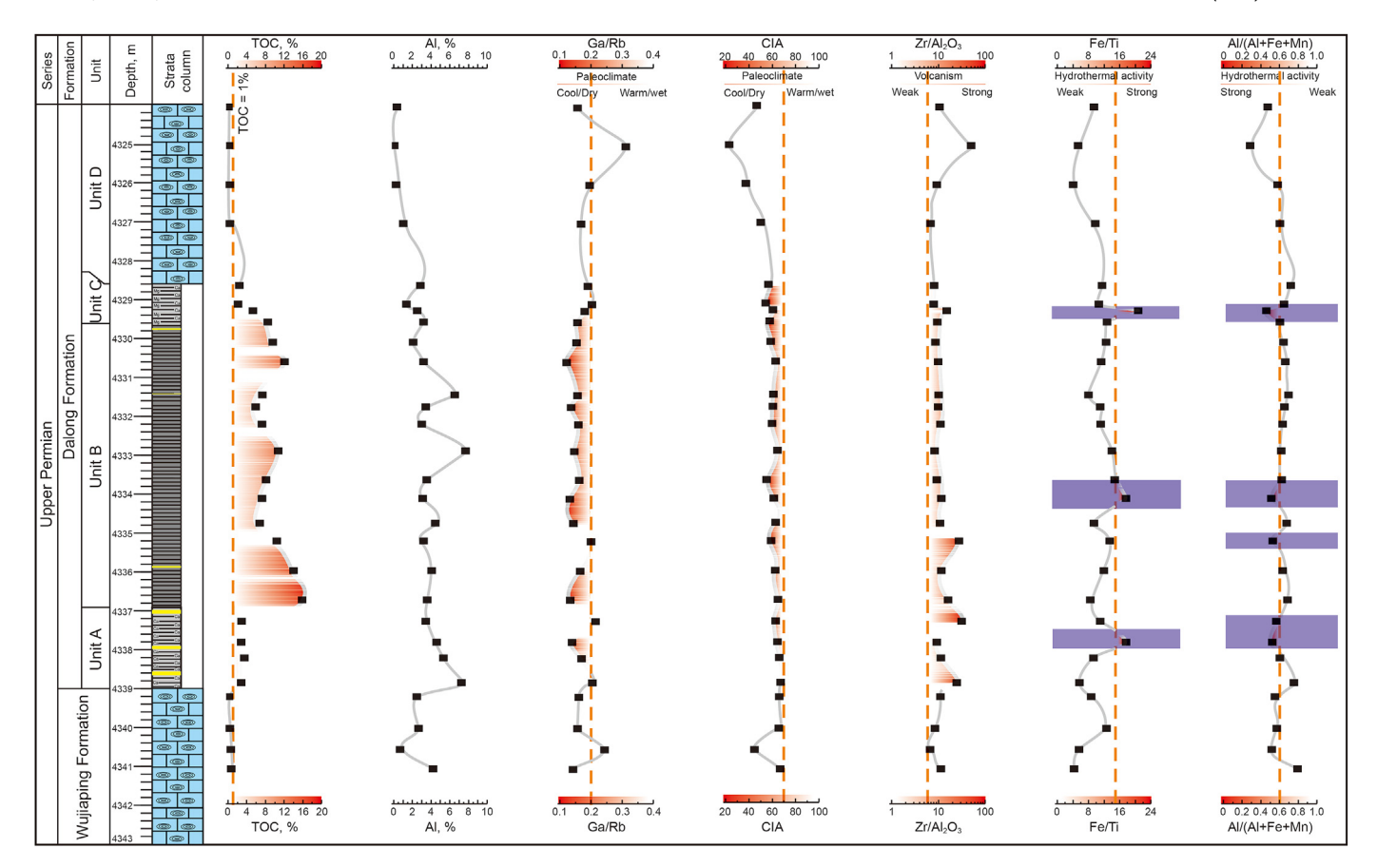
Volcanic eruption materials are often mixed with sediments as fine particles that are unrecognizable to the naked eye, obscuring evidence of volcanism during black shale deposition events (Yang et al., 2022). Gaseous Hg released by volcanic activity is absorbed by organic matter after entering sea water, resulting in Hg enrichment in sediments. Therefore, an abnormally high Hg content can indicate volcanism (Lu et al., 2022). These methods involve the quantification of particular elements (such as Hg, Hg/TOC, and Hg/TS) and their related isotopes (such as <sup>199</sup>Hg), which are common proxies for identifying volcanism (Grasby et al., 2019, 2020; Matsumoto et al., 2021). However, volcanism is not the sole driver of Hg anomalies. Other factors, such as biomass burning, soil erosion, and host minerals, can also lead to abnormal Hg enrichment (Grasby et al., 2019; Yang et al., 2022). Based on numerous bentonite databases worldwide, Yang et al. (2022) proposed that

 $Zr/Al_2O_3 > 6.0$  is an effective proxy for volcanism. The  $Zr/Al_2O_3$  ratios of Units A, B, C, and D ranged from 9.18 to 31.40 (average = 19.15), 8.32 to 27.62 (average = 12.08), 7.90 to 15.11 (average = 10.12), and 6.82 to 50.0 (average = 19.13), respectively. These  $Zr/Al_2O_3$  ratios indicate that the deposition of the black shale in the Dalong Formation at well DY-1H was influenced by volcanism. As illustrated in Fig. 8, the  $Zr/Al_2O_3$  proxy shows a gradual vertical decreasing trend, except for the outlier DY-1H-23 in the Unit D sample. Unit A was affected by strong volcanism, Unit B by moderate volcanism, and Unit C experienced a gradual weakening. The results of the geochemical analysis were consistent with the core observations.

## 6.2.2. Hydrothermal activity records

REEs are not easily affected by diagenesis and are widely used to identify the origin of fine-grained sediments. Modern marine sediment deposits are characterized by LREE depletion, a strong negative Ce anomaly, and a weak negative Eu anomaly. By contrast, hydrothermal vent deposits are distinguished by LREE depletion, Ce anomalies, and strongly positive Eu anomalies. As illustrated in Fig. 9, almost all the samples from Units A, D, C, and D had low REE contents, indicating that the black shale of the Dalong Formation was minimally affected by terrigenous input. The black shales of Units A, B, and C displayed low REE contents, LREE depletion, weak negative Ce anomalies, and weak negative Eu anomalies (Fig. 9(a), (b), and (c)), indicating that they were almost unaffected by hydrothermal activity. However, three samples from Unit D showed an obvious positive Eu anomaly, which may be related to the diagenetic alteration of Fe-Mn oxides in the carbonate rocks (Fig. 9(d)).

The hydrothermal vents of the western Pacific Rise are enriched in Fe and Mn and depleted in Al and Ti. The ratios of Al/(Al + Fe + Mn) and Fe/Ti can be used as proxies for hydrothermal activity. The Fe/Ti ratio of hydrothermal sediments is generally



 $\textbf{Fig. 8.} \ \ Vertical\ variations\ of\ paleoclimate\ proxies\ (CIA, Ga/Rb),\ volcanism\ (Zr/Al_2O_3),\ and\ hydrothermal\ proxies\ (Fe/Ti,\ Al/(Al+Fe+Mn))\ of\ the\ Dalong\ Formation\ in\ the\ well\ DY-1H.$ 

greater than 15, and the Al/(Al + Fe + Mn) ratio is less than 0.6 (Harris et al., 2011). The cross-plot of Fe/Ti vs. Al/(Al + Fe + Mn)helps identify possible hydrothermal input into hydrogenous sediments (Sylvestre et al., 2017; Wang et al., 2020). The AI/(AI + Fe + Mn) ratios of Units A, B, C, and D ranged from 0.52 to 0.75 (average = 0.61), 0.51 to 0.69 (average = 0.63), 0.46 to 0.72 (average = 0.61), and 0.29 to 0.61 (average = 0.49), respectively. As illustrated in Fig. 8, the average Al/(Al + Fe + Mn) values for Units A, B, and C were slightly above the hydrothermal activity threshold of 0.6, whereas the average Fe/Ti values were lower than the threshold of 15. However, some samples still showed signs of hydrothermal activity. As illustrated in Fig. 10(a), although most of the samples from Units A, B, and C fall within the region indicating no hydrothermal activity, some samples fall within the weak hydrothermal activity region, suggesting that hydrogenous sedimentation was the primary driver of the black shales of the Dalong Formation. However, the influence of weak hydrothermal activity should not be entirely dismissed. The lower average Al/(Al + Fe + Mn) ratio in Unit D compared to the threshold value of 0.6 is mainly attributed to the high Mn content in the carbonate rocks, which cannot be easily explained as a result of hydrothermal activity.

#### 6.3. Reconstruction of the paleoenvironmental conditions

## 6.3.1. Paleoclimatic conditions

Paleoclimate indirectly controls organic matter accumulation by influencing chemical weathering intensity, detrital input, and biological assemblages. Numerous geochemical proxies, such as the weathering index (Parker, 1970), chemical index of alteration (CIA) (Nesbitt and Young, 1982), and chemical index of weathering

(Harris et al., 2013), have been applied to paleoclimate reconstruction.

The CIA, proposed by Nesbitt and Young (1982), has low interference and is widely used for paleoclimatic reconstruction (Goldberg and Humayun, 2010; Liu et al., 2022b). Generally, a low CIA (ranging from 50 to 65) indicates a cold and arid climate with weak chemical weathering, an intermediate CIA (ranging from 65 to 85) reflects a warm and humid climate with moderate chemical weathering, and a high CIA (exceeding 85) indicates a hot and humid climate with intense chemical weathering (Nesbitt and Young, 1982). The CIA equation is as follows:

CIA = mole 
$$[Al_2O_3 / (Al_2O_3 + CaO^* + Na_2O + K_2O] \times 100\%$$
 (2)

where CaO\* refers to CaO in silicates only. A correction method was used to eliminate the influence of phosphates (apatite) or CaO-bearing carbonates (calcite and dolomite) (McLennan, 1993). CaO\* was calculated as follows:

$$CaO^* = mole \left[ Cao - \left( P_2O_5 \times \frac{10}{3} \right) \right]$$
 (3)

If mole (Na<sub>2</sub>O)  $\leq$  CaO\*, then CaO\* = Na<sub>2</sub>O, otherwise, CaO\* = CaO. The CIA of Units A, B, and C ranged from 62.85 to 67.13 (average = 65.02), 55.03 to 64.81 (average = 61.04), 54.51 to 60.58 (average = 57.34), respectively. The calculation error for Unit D limestone, which was rich in CaCO<sub>3</sub>, was large, and thus, it is not discussed here. Moreover, the A–CN–K (Al<sub>2</sub>O<sub>3</sub>–(CaO\*+Na<sub>2</sub>O)–K<sub>2</sub>O) diagram was used to correct for the influence of pervasive K-metasomatism (Nesbitt and Young, 1982). The corrected K<sub>2</sub>O (K<sub>2</sub>O<sub>corr</sub>) was calculated as follows:

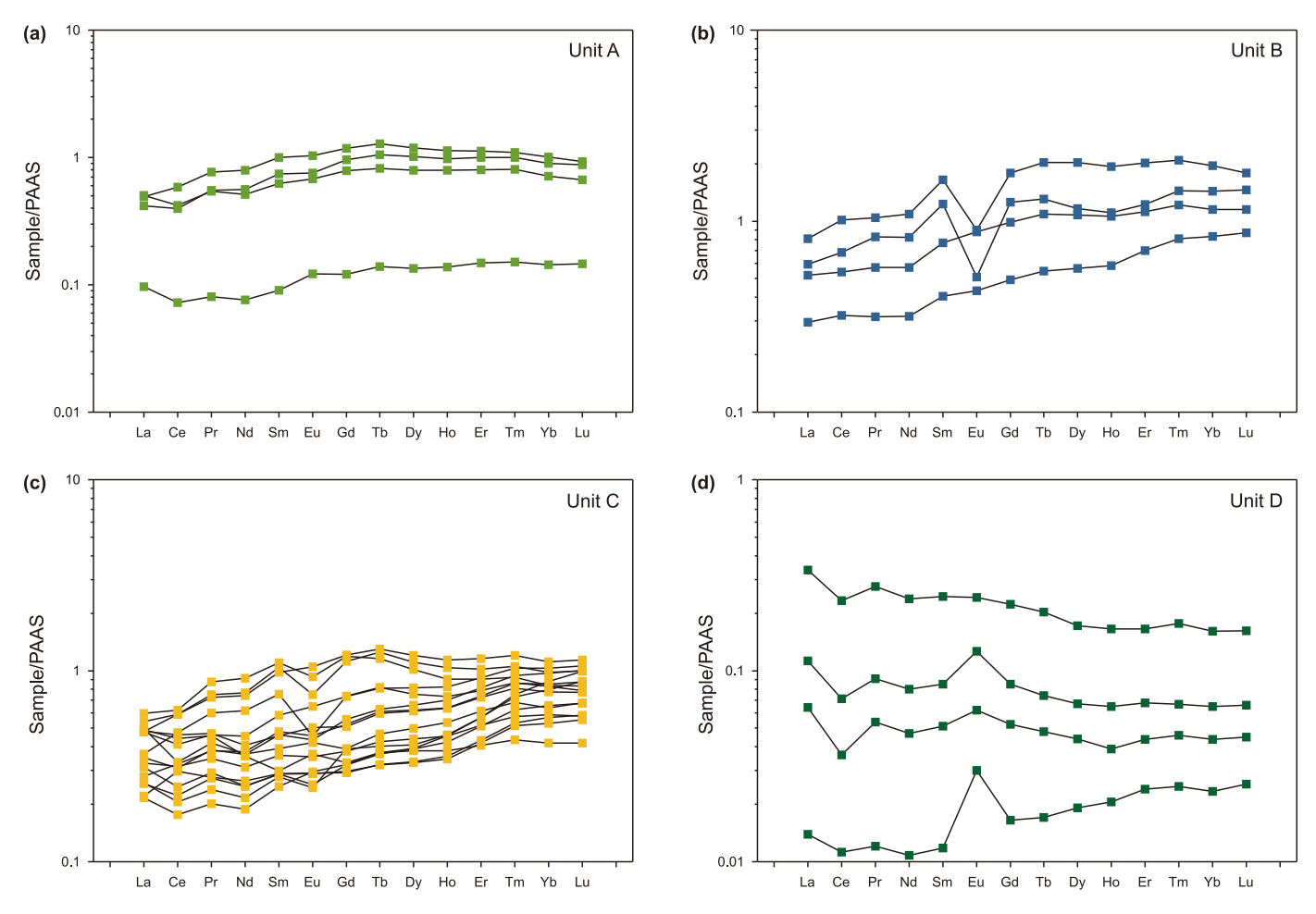


Fig. 9. PAAS-normalized REE patterns of the Dalong Formation's black shales. (a) Unit A, (b) Unit B, (c) Unit C, (d) Unit D.

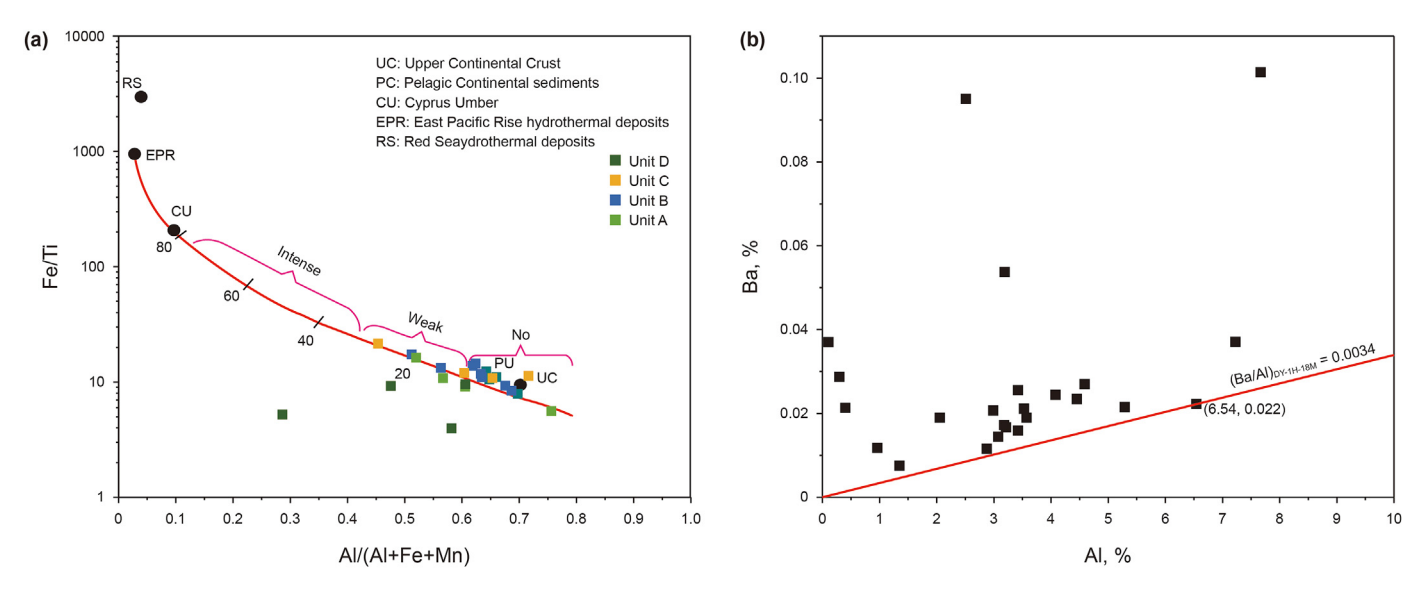


Fig. 10. (a) Fe/Ti vs. Al/(Al + Fe + Mn), cross-plot, modified from Sylvestre et al. (2017). (b) Ba-Al cross-plot of the Dalong Formation's black shales in the well DY-1H.

$$(K_2O)_{corr} = mole \left[ m \times Al_2O_3 + m \times (CaO^* + Na_2O) \right] / (1 - m)$$

$$m = mole \left[ \frac{K_2O}{Al_2O_3 + CaO^* + Na_2O + K_2O} \right]$$

$$(5)$$

The K-metasomatism correction obtained from the A–CN–K diagram is shown in Fig. 11(a). Except for a few samples from Unit A

with CIA values slightly above 65, the vast majority of the Dalong Formation black shale samples had CIA values below 65, indicating that the black shales of the Late Permian Dalong Formation were deposited in a dry environment with a low degree of chemical weathering. As shown in Fig. 8, the CIA proxy decreased vertically, indicating that the paleoclimate gradually became drier. Similar conclusions can be drawn from the Ga/Rb vs. K<sub>2</sub>O/Al<sub>2</sub>O<sub>3</sub> cross-plot (Fig. 11(b)). The increasingly dry climate of the Late Permian and the low degree of chemical weathering may have been related to volcanism. The eruption of the Siberian Large Igneous Province released many greenhouse and toxic gases, leading to global warming, a dry climate, and low chemical weathering.

#### 6.3.2. Paleoredox conditions

A compilation of  $C_{\rm org}/P$  ratios for modern marine systems shows that sedimentary  $C_{\rm org}/P$  ratios are commonly < 50:1 for oxic—suboxic conditions, 50:1—150:1 for suboxic and intermittently anoxic conditions, and > 150:1 for permanently anoxic conditions (Algeo and Ingall, 2007). The  $C_{\rm org}/P$  ratios of Units A, B, C, and D ranged from 25.63 to 43.13 (average = 33.91, n=4), 35.41 to 713.79 (average = 276.65, n=12), 10.60 to 375.61 (average = 180.08, n=4), and 6.80 to 33.65 (average = 17.03, n=4), respectively. As illustrated in Fig. 12, the proxy for  $C_{\rm org}/P$  increased and then decreased vertically. Unit A was deposited under suboxic conditions. Units B and C were deposited under permanent anoxic conditions. Unit D was deposited under oxidizing conditions.

The  $U_{EF}$  ratios of Units A, B, and C ranged from 1.47 to 8.64 (average = 6.67, n = 4), 3.79 to 31.70 (average = 14.01, n = 12), and 18.73 to 32.57 (average = 26.09, n = 4), respectively. The  $M_{OEF}$  ratios of Units A, B, and C ranged from 1.70 to 46.00 (average = 22.32, n = 3, the DY-1H-3 outlier is removed), 27.56 to 250.03 (average = 108.69, n = 12), and 55.89 to 1040.71 (average = 470.37, n = 4), respectively. Unit D is carbonate rock, thus the enrichment factor is ineffective in redox discrimination and will not be discussed. As illustrated in Fig. 12, the  $U_{EF}$  and  $M_{OEF}$  decreased vertically. Unit A exhibited the lowest  $U_{EF}$  and  $M_{OEF}$ , while Units B and C showed significantly higher values. The  $M_{OEF}$  and  $U_{EF}$  of Units B and C were extremely high, indicating anoxic conditions (Fig. 12) (Algeo and Maynard, 2004). The oxidation degree of Unit A was stronger

than that of Units B and C. Mo—U covariation patterns based on enrichment factors (MoEF and UEF) are effective redox proxies for bottom waters (Tribovillard et al., 2006, 2012; Algeo and Tribovillard, 2009). Based on the Mo/U ratio of present SW, the Mo/U ratio of sediments is lower than 0.3  $\times$  SW under oxic conditions, ranges from 0.1  $\times$  SW to 1  $\times$  SW under suboxic conditions, ranges from 1  $\times$  SW to 3  $\times$  SW under anoxic conditions, and exceeds 3  $\times$  SW under euxinic conditions (Tribovillard et al., 2012). As illustrated in Fig. 13(a), the samples from Units A, B, and C fall on the suboxic-anoxic, anoxic, and euxinic spectra of the MoEF—UEF covariation, respectively. Based on the aforementioned discussion of the  $C_{\rm org}/P$ ,  $U_{\rm EF}$ ,  $Mo_{\rm EF}$ , and  $Mo_{\rm EF}$ —UEF covariation patterns, Units A, B and C, and D were deposited under suboxic, anoxic, and oxidizing conditions, respectively.

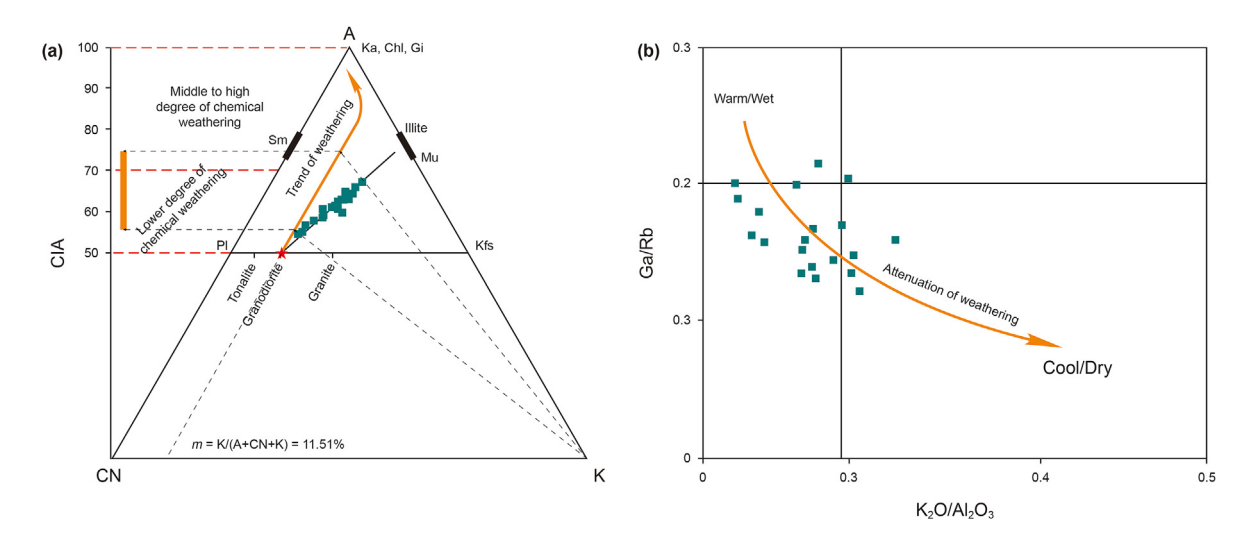
#### 6.3.3. Primary productivity

Various geochemical proxies, such as TOC, carbon and nitrogen isotopes, organic biomarkers, and trace elements (P, Ba, Cu, Ni, Cd, and Zn), have been widely used to evaluate primary productivity (Tribovillard et al., 2006; Algeo et al., 2011; Schoepfer et al., 2015). Biogenic Ba and excess Cu are commonly used proxies for primary productivity (Schoepfer et al., 2015).

Biogenic Ba was determined by calculating the amount of excess Ba  $(Ba_{xs})$  from the expected detrital Ba concentration  $(Ba_{detr})$ , as follows:

$$[Ba_{xs}] = [Ba_{total}] - [Al] \times \left(\frac{Ba}{Al}\right)_{detr}$$
 (6)

We assumed that  $Ba_{bio}$  is equivalent to  $Ba_{xs}$  and that all non-detrital Ba is of biogenic origin. To eliminate the influence of weathering and transportation on Ba, the  $(Ba/Al)_{detr}$  ratio was corrected using an Al vs. Ba cross-plot, where the sample with the lowest Ba/Al ratio was presumed to contain minimal biogenic Ba (Schoepfer et al., 2015). Using this method, the  $(Ba/Al)_{detr}$  ratio was estimated as 0.0034 (Fig. 10(b)). The Ba<sub>bio</sub> of Units A, B, C, and D ranged from 35.53 to 125.46 ppm, 0.49–753.24 ppm, 18.08–865.07 ppm, and 98.38–349.36 ppm, respectively, averaging 79.59 ppm, 135.87 ppm, 335.38 ppm, and 229.48 ppm, respectively. The Ba<sub>bio</sub> values were calculated based on the  $(Ba/Al)_{detr}$  in the



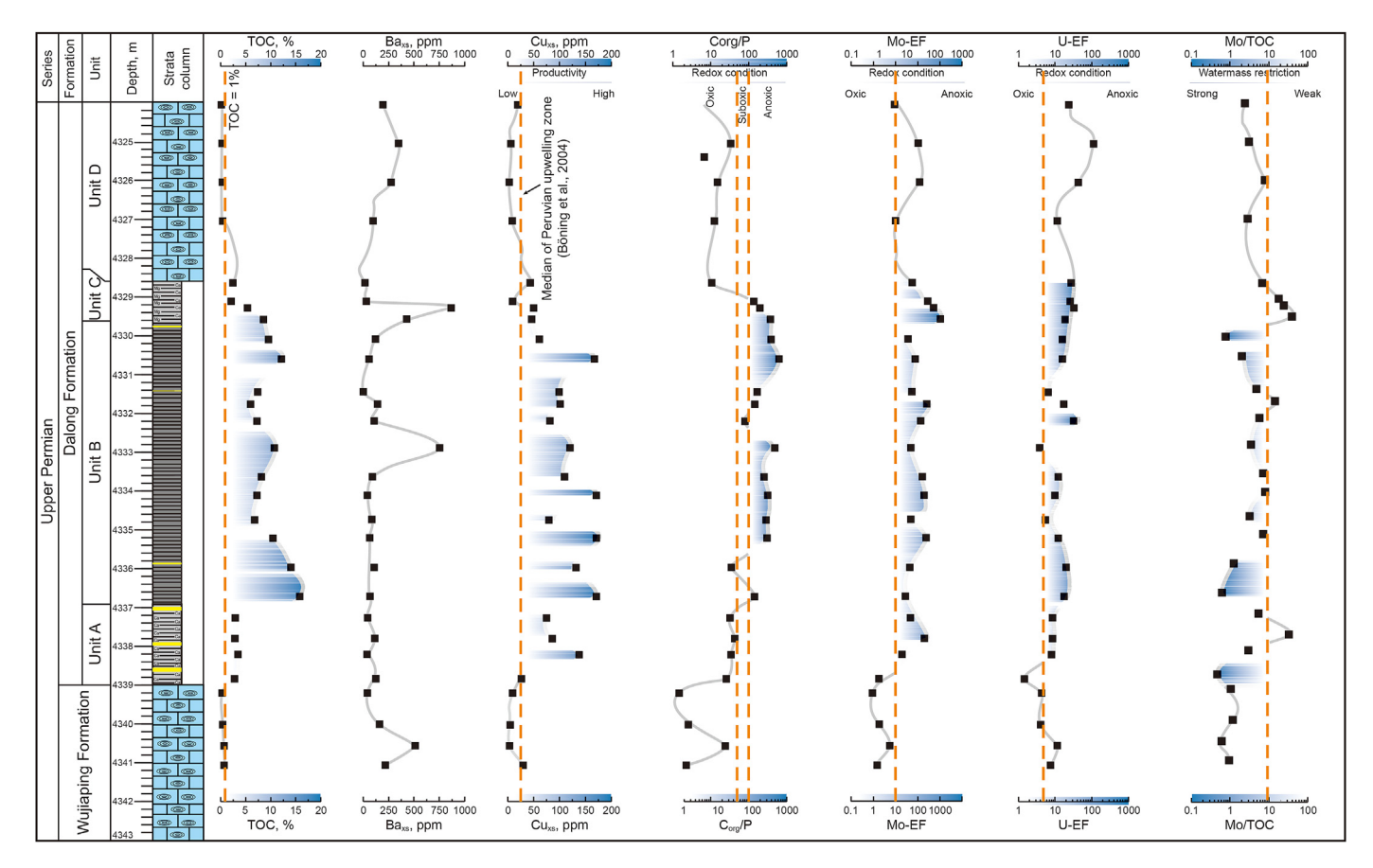
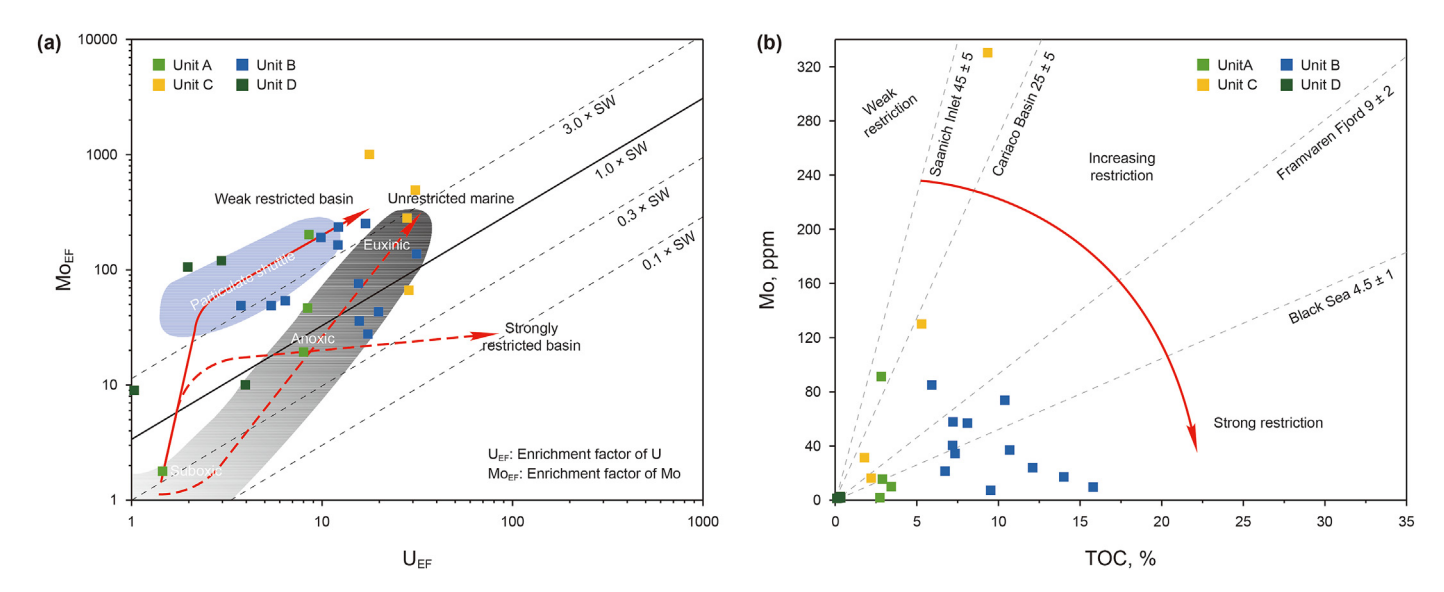


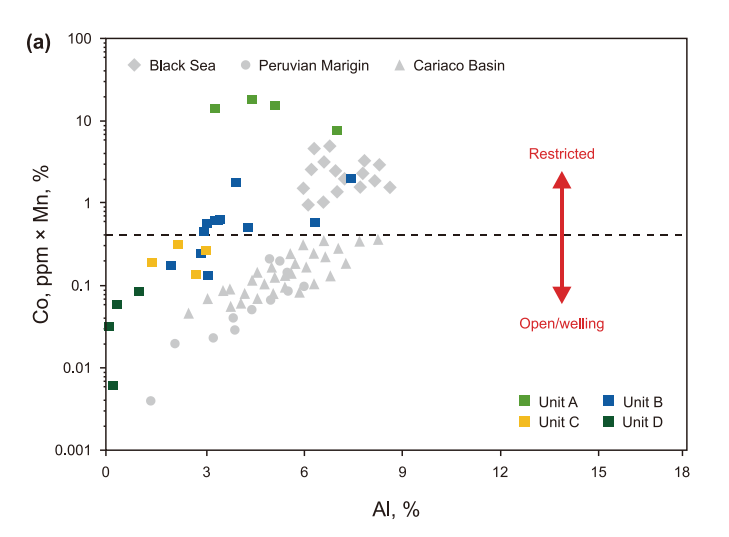
Fig. 12. Vertical variations of primary productivity proxies (TOC, Ba<sub>xs</sub>, Cu<sub>xs</sub>), redox proxies (Mo<sub>EF</sub>, U<sub>EF</sub>, C<sub>org</sub>/P), and water mass restriction (Mo/TOC) of the Dalong Formation in the well DY-1H.



**Fig. 13.** (a) Mo<sub>EF</sub> vs. U<sub>EF</sub> covariation patterns for studied samples. The SW represents present-day seawaters Mo/U molar concentration ratio, molar ratios of ~7.5 for the Pacific and ~7.9 for the Atlantic. The diagonal lines represent multiples (0.1, 0.3, 1, and 3) of the Mo/U ratio of present-day seawater (Algeo and Tribovillard, 2009; Tribovillard et al., 2012). (b) The cross-plot of Mo vs. TOC. Saanich Inlet, Cariaco Basin, Framvaren Fjord, and the black sea are the four modern anoxic marine environments shown by the black dashed lines. The red dashed line indicates an increase in water mass restriction (Algeo and Lyons, 2006) (modified from Rowe et al. (2008)).

upwelling zones of the modern ocean (Murray and Leinen, 1993), which yielded a  $Ba_{bio}$  value of 1350 ppm. Using 1350 ppm as the reference line (Fig. 12), the black shales of the Dalong Formation displayed low  $Ba_{bio}$ , suggesting low primary productivity. However,

given that Ba may be affected by the recycling of these elements from anoxic-euxinic sediments into the water column (Bottrell and Newton, 2006; Algeo et al., 2011; Schoepfer et al., 2015), black shales deposited under anoxic conditions (Fig. 12) may yield low



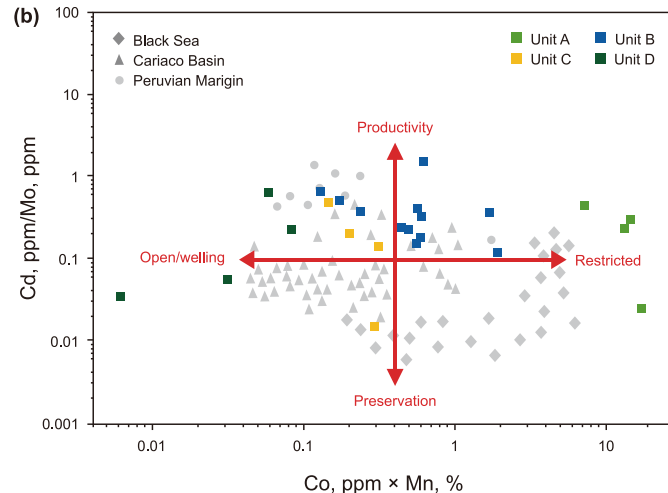


Fig. 14. (a) Cross-plots of Co (ppm) × Mn (%) ratios versus Al (%) (modified from Sweere et al., 2016). (b) Cross-plots of Cd/Mo ratios versus Co (ppm) × Mn (%) (modified from Sweere et al., 2016).

Ba<sub>bio</sub> values. Therefore, the Ba<sub>bio</sub> values of the black shales in the Dalong Formation may have been significantly underestimated.

Excess Cu ( $Cu_{xs}$ ) was calculated by subtracting the detrital Cu fraction ( $Cu_{detr}$ ) from the total Cu fraction ( $Cu_{total}$ ). The  $Cu_{xs}$  content was calculated as follows:

$$[Cu_{xs}] = [Cu_{total}] - [Al] \times \left(\frac{Cu}{Al}\right)_{detr}$$
(7)

We assumed a detrital Cu/Al ratio of 0.00031 based on the average Cu and Al concentrations in the upper continental crust (Mclennan, 2001). The  $\mathrm{Cu_{xs}}$  of Units A, B, C, and D ranged from 26.21 to 137.83 ppm (median = 80.64 ppm; n=4), 61.12–171.47 ppm (median = 114.89 ppm; n=12), 9.35–50.03 ppm (median = 44.67 ppm; n=4), and 3.16–19.16 ppm (median = 7.66 ppm; n=4), respectively. Units A and B exhibited high  $\mathrm{Cu_{xs}}$ , indicating high productivity. Unit C exhibited moderate productivity, whereas Unit D showed low productivity. As illustrated in Fig. 12, the  $\mathrm{Cu_{xs}}$  increased and then decreased vertically. Unit B exhibited the highest productivity, followed by Units A, C, and D.

## 6.3.4. Paleogeographic and hydrographic environment

Paleogeography and hydrological conditions indirectly affect primary productivity, redox conditions, marine stratification, and biogeochemical cycles by influencing seafloor topography, upwelling, and terrigenous inputs (Algeo and Rowe, 2012). Molybdenum (Mo) in sediments is mainly controlled by redox conditions (Rowe et al., 2008). However, the transfer of Mo to sediments under anoxic conditions depends on the concentration of deposited organic matter and the degree of water mass restriction (Algeo and Rowe, 2012). Mo/TOC ratios are commonly used to evaluate the degree of water mass restriction under anoxic conditions (Algeo and Rowe, 2012; Li et al., 2017) with Mo/TOC ratios lower than  $15 \times 10^{-4}$ , between  $15 \times 10^{-4}$  and  $35 \times 10^{-4}$ , and greater than  $35\times 10^{-4}$  indicating strongly restricted, moderately restricted, and unrestricted basins, respectively (Algeo and Lyons, 2006). The Mo/ TOC ratios of Units A, B, C, and D ranged from 0.46 to  $32.36 \times 10^{-4}$ (average =  $10.29 \times 10^{-4}$ , n = 4), 0.62 to  $14.42 \times 10^{-4}$  (average =  $4.87 \times 10^{-4}$ , n = 12), 6.72 to  $38.93 \times 10^{-4}$  (average =  $21.91 \times 10^{-4}$ , n = 4), and 2.42 to  $7.84 \times 10^{-4}$ (average =  $4.04 \times 10^{-4}$ , n = 4), respectively. As illustrated in Fig. 13(b), most samples from Units A and B fall within the region of restriction, with Unit A showing a higher degree of restriction than Unit B. All samples from Unit C fall within the region of weak restriction. The TOC of Unit D is less than 1%; therefore, the Mo/TOC ratio is not meaningful for identifying the hydrographic environment.

A study of the migration of Mn and Co in the modern marine water column showed that Mn is more soluble (Sweere et al., 2016), whereas sediments efficiently absorb Co under conditions of intense reduction (Erickson and Helz, 2000; Vorlicek et al., 2004; Tribovillard et al., 2006; Little et al., 2015). Accordingly, Co (ppm) × Mn (%) cross-plots have been proposed to distinguish between restriction and open/upwelling environments (Sweere et al., 2016). This has been verified in the discrimination of modern restricted basins (including the Black Sea) and continental margin upwelling areas (such as the Peruvian marginal sea) (Fig. 14). The Co (ppm)  $\times$  Mn (%) of Units A, B, C, and D ranged from 7.21 to 17.30  $\times$  10<sup>-4</sup> (average = 13.12  $\times$  10<sup>-4</sup>, n = 4), 0.13 to  $1.90 \times 10^{-4}$  (average =  $0.67 \times 10^{-4}$ , n = 12), 0.14 to 0.34  $\times 10^{-4}$ (average =  $0.24 \times 10^{-4}$ , n = 4), and 0.006 to  $0.08 \times 10^{-4}$  (average =  $0.04 \times 10^{-4}$ , n = 4), respectively. As shown in Fig. 14(a), all samples from Unit A fall within the region of strong restriction. Seventy-five percent of the samples from Unit B fall within the restriction region, whereas 25% are affected by upwelling. All samples from Units C and D are in the open/upwelling area, with the degree of openness in Unit D being higher than that in Unit C. Based on the aforementioned discussion of Mo/TOC ratios and cross-plots of Co (ppm)  $\times$  Mn (%) ratios versus Al (%), the hydrographic environment gradually shifted from restriction to open/ upwelling from Unit A to Unit D. The paleogeographic and hydrographic environments are closely related to the sedimentarytectonic evolution of the K-L intracratonic sag. During the deposition of Unit A, a shallow and restricted sag formed at the northern margin of the Sichuan Basin under weak extension, marking the rudimentary development of the K-L intracratonic sag. The relatively shallow water of the sag limited access to the open sea. During the deposition of Unit B, the K-L intracratonic sag broadened and deepened with increased extensional activity. As sea levels rose slowly, the sag became weakly connected to the open sea. During the deposition of Unit C, the K-L intracratonic sag gradually shrank with weakening extensional activity, and the rising sea level created a stronger connection between the sag and the open sea. By the time of Unit D's deposition, extensional activity had ceased, and the K-L intracratonic sag had nearly disappeared.

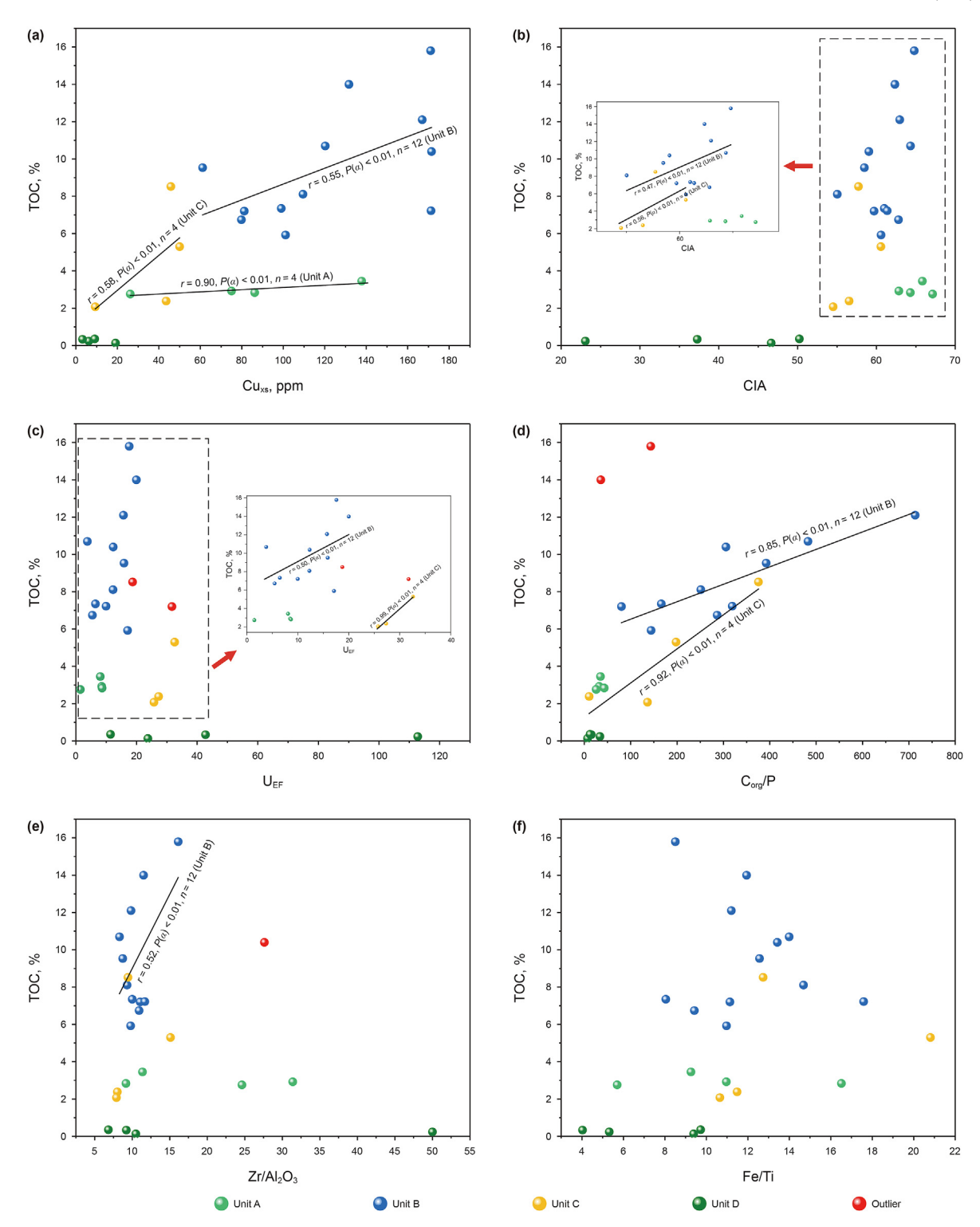


**Fig. 15.** Relationships between TOC contents and (**a**) primary productivity proxy (Cu<sub>xs</sub>), (**b**) paleoclimatic conditions (CIA), (**c**, **d**) paleoredox conditions proxies (U<sub>EF</sub> and C<sub>org</sub>/P), (**e**) volcanism proxy (Zr/Al<sub>2</sub>O<sub>3</sub>), and (**f**) hydrothermal activity proxy (Fe/Ti).

## 6.4. Models for organic matter accumulation

The Sichuan Basin, located in the eastern Paleo-Tethys region of the multi-island-oceanic system (Yu et al., 2021), formed the K-L intracratonic sag (Fig. 1) under the influence of Emei taphrogenesis during the Late Permian (Liu et al., 2021b). The location, far from old land and subject to low chemical weathering due to the dry

climate, rendered the sag almost impervious to terrigenous input, resulting in clear water conditions. Clear water facilitates the penetration of sunlight, increasing the depth of the euphotic zone. Under weak extension, the K-L intracratonic sag had a moderate depth, placing it almost entirely within the euphotic zone. Good light conditions promoted the flourishing of lower benthic plants (such as thread-leaf plants and multicellular benthic macroalgae).

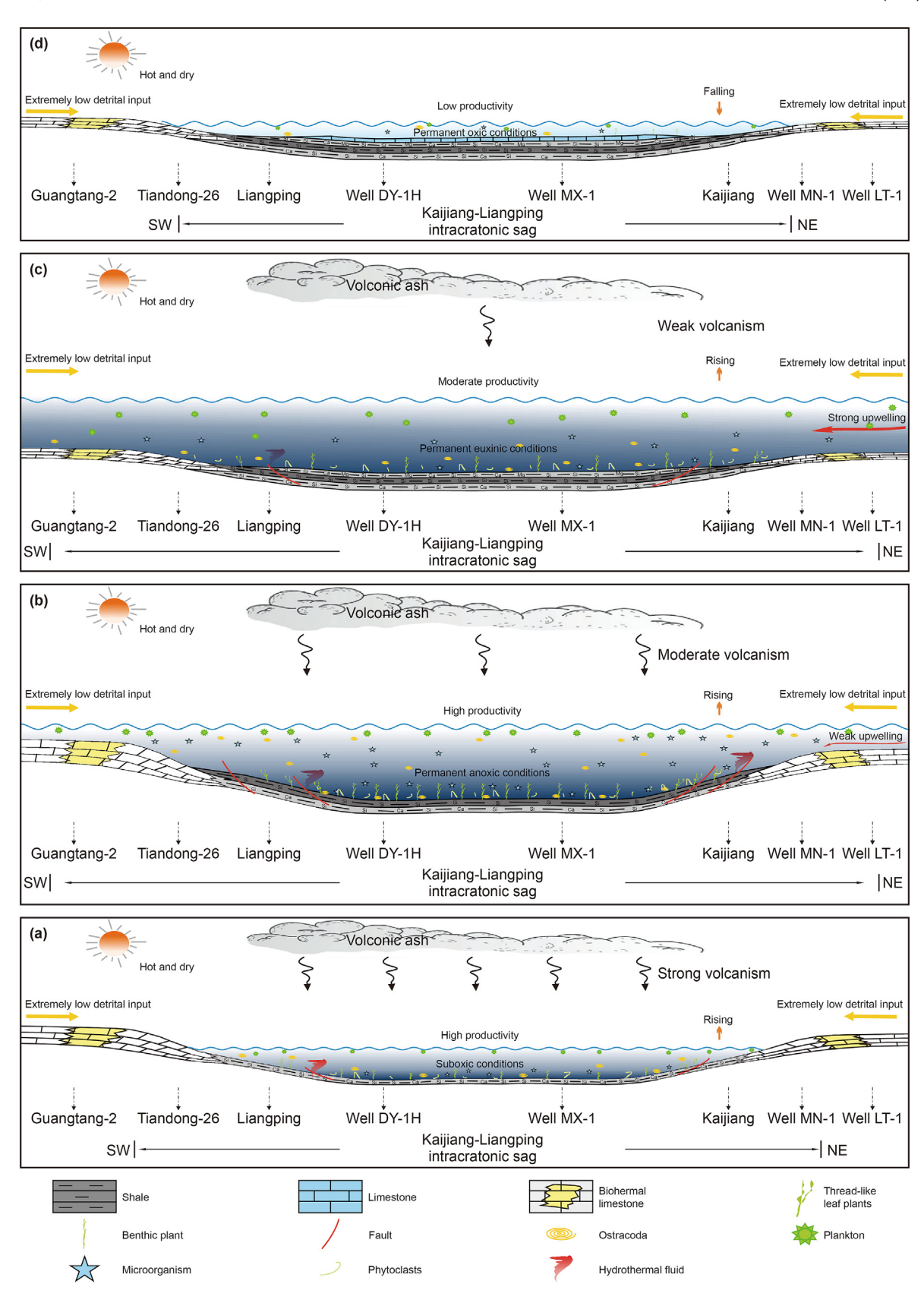


Fig. 16. Organic matter accumulation model of the Dalong Formation in well DY-1H under clear water conditions. For the location of wells and cities, see Fig. 1(c). (a) Unit A, (b) Unit B, (c) Unit C, (d) Unit D.

During diagenesis, dead benthic plants gradually transformed into exinite- and vitrinite-rich Type II<sub>2</sub> kerogen. The production and preservation of lower benthic plants in the K-L intracratonic sag controlled organic matter accumulation in the black shales of the Dalong Formation in the Sichuan Basin under clear water conditions.

#### 6.4.1. Accumulation model for unit A's organic matter

During the deposition of Unit A, a shallow and restricted inland basin formed at the northern margin of the Sichuan Basin under weak extension, marking the early development of the K-L intracratonic sag. The relatively shallow water of the sag prevented access to the open sea. At this time, the strongly restricted sag intermittently exchanged gas with the atmosphere, causing oxygen to dissolve in the SW, resulting in suboxic bottom waters. The eruption of the Siberian Large Igneous Province introduced volcanic ash to the K-L intracratonic sag. The fertilization effect of volcanic ash led to eutrophication, promoting the flourishing of lower benthic plants and increasing productivity (Fig. 14(b)). The primary productivity proxy, Cuxs, was strongly and linearly correlated with TOC (r = 0.90, P( $\alpha$ ) < 0.01, n = 4, Fig. 15(a)). Other proxies (such as Zr/Al<sub>2</sub>O<sub>3</sub>, Fe, Ti, CIA, U<sub>EF</sub>, and C<sub>org</sub>/P) showed no linear correlation with TOC (Fig. 15). This provides compelling evidence that the flourishing of benthic plants provided a substantial material basis for organic matter accumulation in Unit A. Compared to the anoxic conditions, bacterial decomposition is generally stronger under suboxic conditions, which is often not conducive to organic matter preservation. However, the exinite- and vitrinite-rich Type II<sub>2</sub> kerogen in Unit A. derived from benthic plants, was rich in aromatic compounds, had a low H/C ratio, and was difficult to decompose, making it well-preserved even under suboxic conditions. Therefore, the flourishing of benthic plants, which provided abundant exinite- and vitrinite-rich Type II<sub>2</sub> kerogen, is the dominant factor controlling the organic matter accumulation of black shales in Unit An under suboxic conditions (Fig. 16(a)).

### 6.4.2. Accumulation model for unit B's organic matter

During the deposition of Unit B, the K-L intracratonic sag broadened and deepened with the strengthening of extensional activities. As sea levels rose slowly, the sag became weakly connected to the open sea. Under restricted conditions, anoxic environments prevailed due to the limited exchange between the water mass and the adjoining ocean (Li et al., 2017; Xia et al., 2024; Yan et al., 2015). The formation of a low-salinity surface water layer accelerated water column stratification, further blocking oxygen exchange between the bottom water and the atmosphere and intensifying anoxic conditions (Xiao et al., 2019). Weak upwelling from the open sea intermittently carried nutrients into the sag, and volcanism gradually decreased in intensity. Under the combined influence of weak upwelling and moderate volcanism, abundant nutrients promoted the growth of benthic plants, further increasing productivity (Figs. 14(b) and 16(b)). The primary productivity proxy  $(Cu_{xs})$  showed a moderately positive correlation with TOC (r = 0.55,  $P(\alpha) < 0.01$ , n = 12, Fig. 15(a)), as did the paleoclimatic condition proxy (CIA) (r = 0.47, P( $\alpha$ ) < 0.01, n = 12, Fig. 15(b)). The volcanism proxy (Zr/Al<sub>2</sub>O<sub>3</sub>) exhibited a moderately positive correlation with TOC (r = 0.52, P( $\alpha$ ) < 0.01, n = 11, Fig. 15(e)), and the paleoredox condition proxies (C<sub>org</sub>/P, U<sub>EF</sub>) showed strongly and moderately positive correlations with TOC, respectively (r = 0.85, P( $\alpha$ ) < 0.01, n= 10, r = 0.50,  $P(\alpha)$  < 0.01, n = 12, Fig. 15(d) and (c)). This indicates that high productivity and anoxic conditions jointly promoted organic matter accumulation in Unit B's black shales. The flourishing benthic plants increased productivity, while anoxic conditions ensured excellent organic matter preservation. Additionally, the exinite- and vitrinite-rich Type II<sub>2</sub> kerogen was resistant to decomposition and easily preserved, further aiding in organic matter preservation.

#### 6.4.3. Accumulation model for unit C's organic matter

During the deposition of Unit C, the K-L intracratonic sag gradually shrank due to weakening extensional activities. As sea levels rose rapidly, the sag became strongly connected to the open sea. Rising sea levels resulted in less frequent water column overturning, promoting redox stratification. Strong upwelling from the open sea introduced some nutrients into the sag, but volcanism weakened. Compared with observation in Units A and B, the weaker volcanism in Unit C reduced nutrient input, inhibiting the growth of benthic plants and lowering productivity from high to moderate levels (Figs. 14(b) and 16(c)). The primary productivity proxy (Cuxs) exhibited a moderately positive correlation with TOC  $(r = 0.58, P(\alpha) < 0.01, n = 4, Fig. 15(a))$ , as did the paleoclimatic condition proxy (CIA) (r = 0.56, P( $\alpha$ ) < 0.01, n = 12, Fig. 15(b)). The paleoredox condition proxies (C<sub>org</sub>/P, U<sub>EF</sub>) showed strongly positive correlations with TOC (r = 0.92,  $P(\alpha) < 0.01$ , n = 4; r = 0.99,  $P(\alpha) < 0.01$ 0.01, n = 3, Fig. 15(d) and (c)). This suggests that anoxic conditions influenced organic matter accumulation in Unit C, despite the moderate productivity levels. Generally, it is challenging to form shale rich in ultrahigh organic matter under moderate productivity, even in oxidizing conditions. The ultrahigh organic matter accumulation in Unit C can be attributed to the exinite- and vitriniterich Type II<sub>2</sub> kerogen. Although benthic plant growth was reduced in Unit C, the anoxic bottom water and the kerogen's resistance to decomposition ensured the preservation of the limited organic matter.

#### 6.4.4. Accumulation model for unit D's organic matter

During the deposition of Unit D, extensional activities ceased, and the K-L intracratonic sag nearly disappeared. A dramatic drop in sea level and sag fading led to anoxic conditions being replaced with oxic conditions (Fig. 16(d)). The cessation of volcanism and upwelling triggered a sharp decline in productivity. The number of benthic plants decreased dramatically. The oxidized bottom water and the reduction in benthic plants played crucial roles in the sharp decline of organic matter in Unit D.

## 7. Conclusion

- (1) The black shales of the Dalong Formation contain ultrahigh organic matter. Petrological and geochemical analyses of well DY-1H revealed four distinct units within the Dalong Formation: A, B, C, and D, with average TOC contents of 3.00%, 9.59%, 4.57%, and 0.27%, respectively.
- (2) The kerogen maceral analysis of Units A, B, and C's black shales shows that the kerogen primarily comprises exinite-and vitrinite-rich Type Il<sub>2</sub> kerogen. Benthic plants growing in clear waters may be the primary source of organic matter.
- (3) The paleoenvironment of the Dalong Formation exhibits vertical heterogeneity. Unit A features shallow water, suboxic conditions, strong volcanism, and high productivity. Restricted ocean circulation, anoxic conditions, weak upwelling, moderate volcanism, and high productivity characterize Unit B. Unit C features anoxic conditions, strong upwelling, weak volcanism, and moderate productivity. Oxic conditions and low productivity define Unit D.
- (4) The flourishing of benthic plants, a significant source of Type Il<sub>2</sub> kerogen that resists decomposition and favors preservation, is the dominant factor controlling the ultrahigh organic matter accumulation in Units A, B, and C's black shales under clear water conditions.

(5) The oxidized bottom water and the decrease in benthic plants played crucial roles in the sharp decline in organic matter in Unit D.

## **Declaration of competing interest**

The authors declare that they have no known competing financial interests or personal relationships that could have appeared to influence the work reported in this paper.

#### **CRediT authorship contribution statement**

**Guo-Dong Xia:** Writing — original draft, Methodology, Investigation. **Yue-Hao Ye:** Writing — review & editing, Supervision, Conceptualization. **Shu-Gen Liu:** Project administration, Funding acquisition. **Hua Wang:** Resources, Project administration. **Kun Jiao:** Writing — review & editing. **Jin-Min Song:** Supervision, Methodology, Formal analysis. **Zhi-Wu Li:** Validation, Investigation, Formal analysis. **Wei Chen:** Investigation. **Ying Ming:** Project administration. **Xiao-Gang Ma:** Methodology. **Heng Wang:** Visualization. **Chun-Qiao Yan:** Investigation. **Yun Zeng:** Writing — review & editing, Writing — original draft.

#### **Acknowledgments**

This study was supported by the National Natural Science Foundation of China (Grant Nos. U2344209, U42230310, U42207293) and Natural Science Foundation of Sichuan Province, China (Grant No. 2023NSFSC0262). We acknowledge three anonymous reviewers for their valuable comments and suggestions, which greatly improve the quality of the manuscript.

#### References

- Algeo, T.J., Ingall, E., 2007. Sedimentary Corg: P ratios, paleocean ventilation, and Phanerozoic atmospheric pO<sub>2</sub>. Palaeogeogr. Palaeoclimatol. Palaeoecol. 256, 130–155. https://doi.org/10.1016/j.palaeo.2007.02.029.
- Algeo, T.J., Kuwahara, K., Sano, H., Bates, S., Lyons, T., Elswick, E., Hinnov, L., Ellwood, B., Moser, J., Maynard, J.B., 2011. Spatial variation in sediment fluxes, redox conditions, and productivity in the Permian—Triassic Panthalassic Ocean. Palaeogeogr. Palaeoclimatol. Palaeoecol. 308, 65–83. https://doi.org/10.1016/ipalaeo.2010.07.007.
- Algeo, T.J., Lyons, T.W., 2006. Mo-total organic carbon covariation in modern anoxic marine environments: implications for analysis of paleoredox and paleohydrographic conditions. Paleoceanography 21, PA1016. https://doi.org/10.1029/ 2004PA001112.
- Algeo, T.J., Maynard, J.B., 2004. Trace-element behavior and redox facies in core shales of Upper Pennsylvanian Kansas-type cyclothems. Chem. Geol. 206, 289–318. https://doi.org/10.1016/j.chemgeo.2003.12.009.
- Algeo, T.J., Rowe, H., 2012. Paleoceanographic applications of trace-metal concentration data. Chem. Geol. 324, 6–18. https://doi.org/10.1016/j.chemgeo.2011.09.002.
- Algeo, T.J., Tribovillard, N., 2009. Environmental analysis of paleoceanographic systems based on molybdenum—uranium covariation. Chem. Geol. 268, 211–225. https://doi.org/10.1016/j.chemgeo.2009.09.001.
- Bottrell, S.H., Newton, R.J., 2006. Reconstruction of changes in global sulfur cycling from marine sulfate isotopes. Earth Sci. Rev. 75, 59–83. https://doi.org/10.1016/ i.earscirey.2005.10.004.
- Carey, F., Sundberg, R., 2001. Advanced organic chemistry. Part B: reactions and synthesis. In: Molecules, fourth ed., vol. 6
- Chapman, T., Milan, L.A., Metcalfe, I., Blevin, P.L., Crowley, J., 2022. Pulses in silicic arc magmatism initiate end-Permian climate instability and extinction. Nat. Geosci. 15, 411. https://doi.org/10.1038/s41561-022-00934-1.
  Chen, B., Li, Y., Deng, T., Dong, S., Zhao, S., Hu, W., 2019. The sedimentary envi-
- Chen, B., Li, Y., Deng, T., Dong, S., Zhao, S., Hu, W., 2019. The sedimentary environment and organic matter enrichment pattern of Xujiahe Formation shale in the Late Triassic Longmenshan foreland basin, SW China. Chin. J. Geol. 54, 434–451. https://doi.org/10.12017/dzkx.2019.028 (in Chinese).
- Cocks, L.R.M., Torsvik, T.H., 2007. Siberia, the wandering northern terrane, and its changing geography through the Palaeozoic. Earth Sci. Rev. 82, 29–74. https://doi.org/10.1016/j.earscirev.2007.02.001.
- Dal Corso, J., Song, H.J., Callegaro, S., Chu, D.L., Sun, Y.D., Hilton, J., Grasby, S.E., Joachimski, M.M., Wignall, P.B., 2022. Environmental crises at the Permian-

- Triassic mass extinction. Nat. Rev. Earth Environ. 3, 197–214. https://doi.org/10.1038/s43017-021-00259-4.
- Demaison, G.J., Moore, G.T., 1980. Anoxic environments and oil source bed genesis. Org. Geochem. 2, 9–31. https://doi.org/10.1016/0146-6380(80)90017-0.
- Du, X.B., Jia, J.X., Zhao, K., Shi, J.C., Shu, Y., Liu, Z.H., Duan, D., 2021. Was the volcanism during the Ordovician-Silurian transition in South China actually global in extent? Evidence from the distribution of volcanic ash beds in black shales. Mar. Petrol. Geol. 123, 104721. https://doi.org/10.1016/j.marpetgeo.2020.104721.
- Duggen, S., Croot, P., Schacht, U., Hoffmann, L., 2007. Subduction zone volcanic ash can fertilize the surface ocean and stimulate phytoplankton growth: evidence from biogeochemical experiments and satellite data. Geophys. Res. Lett. 34, L01612. https://doi.org/10.1029/2006GL027522.
- Elrick, M., Polyak, V., Algeo, T.J., Romaniello, S., Asmerom, Y., Herrmann, A.D., Anbar, A.D., Zhao, L., Chen, Z.Q., 2017. Global-ocean redox variation during the middle-late Permian through Early Triassic based on uranium isotope and Th/U trends of marine carbonates. Geology 45, 163–166. https://doi.org/10.1130/G38585.1.
- Ercegovac, M., Kostic, A., 2006. Organic facies and palynofacies: nomenclature, classification and applicability for petroleum source rock evaluation. Int. J. Coal Geol. 68 (1–2), 70–78. https://doi.org/10.1016/j.coal.2005.11.009.
- Geol. 68 (1–2), 70–78. https://doi.org/10.1016/j.coal.2005.11.009. Erickson, B.E., Helz, G.R., 2000. Molybdenum(VI) speciation in sulfidic waters: stability and lability of thiomolybdates. Geochem. Cosmochim. Acta 64, 1149–1158. https://doi.org/10.1016/S0016-7037(99)00423-8.
- Farabegoli, E., Perri, M.C., Posenato, R., 2007. Environmental and biotic changes across the Permian-Triassic boundary in western Tethys: the Bulla parastratotype, Italy. Global Planet. Change 55, 109–135. https://doi.org/10.1016/ i.gloplacha.2006.06.009.
- Fedo, C.M., Nesbitt, H.W., Young, G.M., 1995. Unraveling the effects of potassium metasomatism in sedimentary rocks and paleosols, with implications for paleoweathering conditions and provenance. Geology 23, 921–924. https://doi.org/10.1130/0091-7613(1995)023<0921:UTEOPM>2.3.CO;2.
- Fu, X., Qin, J., Tenger, Wang, X., 2010. Evaluation on Dalong Formation source rock in the north Sichuan Basin. Petroleum Geology & Experiment 32 (6), 566–571. https://doi.org/10.11781/sysydz201006566 (in Chinese).
- Goldberg, K., Humayun, M., 2010. The applicability of the chemical index of alteration as a paleoclimatic indicator: an example from the permian of the parana basin, Brazil. Palaeogeogr. Palaeoclimatol. Palaeoecol. 293, 175–183. https://doi.org/10.1016/j.palaeo.2010.05.015.
- Grasby, S.E., Liu, X.J., Yin, R.S., Ernst, R.E., Chen, Z.H., 2020. Toxic mercury pulses into late Permian terrestrial and marine environments. Geology 48, 830–833. https://doi.org/10.1130/G47295.1.
- Grasby, S.E., Them, T.R., Chen, Z.H., Yin, R.S., Ardakani, O.H., 2019. Mercury as a proxy for volcanic emissions in the geologic record. Earth Sci. Rev. 196, 102880. https://doi.org/10.1016/j.earscirev.2019.102880.
- Guo, J., Hu, G., He, K., Mi, J., Tian, L., He, F., Guo, C., Lu, M., 2023. Geochemical characteristics and sedimentary environment of source rocks of Permian Dalong Formation in northern Sichuan Basin. Lithologic Reservoirs. 35, 139–152. https://doi.org/10.12108/yxyqc.20230514 (in Chinese).
- Hao, F., Guo, T.L., Zhu, Y.M., Cai, X.Y., Zou, H.Y., Li, P.P., 2008. Evidence for multiple stages of oil cracking and thermochemical sulfate reduction in the Puguang gas field, Sichuan Basin, China. AAPG Bull. 92, 611–637. https://doi.org/10.1306/ 01210807090.
- Harris, N.B., Miskimins, J.L., Mnich, C.A., 2011. Mechanical anisotropy in the woodford shale, permian basin: origin, magnitude, and scale. Lead. Edge 30, 284–291. https://doi.org/10.1190/1.3567259.
- Harris, N.B., Mnich, C.A., Selby, D., Korn, D., 2013. Minor and trace element and Re-Os chemistry of the Upper Devonian Woodford Shale, Permian Basin, west Texas: insights into metal abundance and basin processes. Chem. Geol. 356, 76–93. https://doi.org/10.1016/j.chemgeo.2013.07.018.
- Höld, I.M., Brussee, N.J., Schouten, S., Damsté, J.S.S., 1998. Changes in the molecular structure of a Type II-S kerogen (Monterey Formation, USA) during sequential chemical degradation. Org. Geochem. 29, 1403—1417. https://doi.org/10.1016/ S0146-6380(98)00158-2.
- Hu, G., He, F., Mi, J., Yuan, Y., Guo, J., 2021. The geochemical characteristics, distribution patterns, and gas exploration potential of marine source rocks in northwest Sichuan Basin. Nat. Gas Geosci. 32, 319–333. https://doi.org/10. 11764/j.issn.1672-1926.2021.01.013 (in Chinese).
- Huey, R.B., Ward, P.D., 2005. Hypoxia, global warming, and terrestrial Late Permian extinctions. Science 308, 398–401. https://doi.org/10.1126/science.1108019.
- Irwin, M.L., 1965. General theory of epeiric clear water sedimentation. AAPG (Am. Assoc. Pet. Geol.) Bull. 49, 445–459. https://doi.org/10.1306/A6633632-16C0-11D7-8645000102C1865D.
- Lee, C.T.A., Jiang, H.H., Ronay, E., Minisini, D., Stiles, J., Neal, M., 2018. Volcanic ash as a driver of enhanced organic carbon burial in the Cretaceous. Sci. Rep. 8, 4197. https://doi.org/10.1038/s41598-018-22576-3.
- Li, P., Hao, F., Guo, X., Zou, H., Yu, X., Wang, G., 2015. Processes involved in the origin and accumulation of hydrocarbon gases in the Yuanba gas field, Sichuan Basin, southwest China. Mar. Petrol. Geol. 59, 150–165. https://doi.org/10.1016/ j.marpetgeo.2014.08.003.
- Li, P., Liu, Q., Bi, H., Meng, Q., 2021. Analysis of the difference in organic matter preservation in typical lacustrine shale under the influence of volcanism and transgression. Acta Geol. Sin. 95, 632–642 https://doi.org/10.19762/j.cnki.dizhixuebao.2021123 (in Chinese).

Li, Y., Zhang, T., Ellis, G.S., Shao, D., 2017. Depositional environment and organic matter accumulation of upper ordovician—lower silurian marine shale in the upper Yangtze platform, south China. Palaeogeogr. Palaeoclimatol. Palaeoecol. 466, 252–264. https://doi.org/10.1016/j.palaeo.2016.11.037.

- Lian, Z., Haiqiang, Z., Jin, W., Junhua, H., Xinong, X., 2008. Assessment on redox conditions and organic burial of siliciferous sediments at the latest permian Dalong Formation in shangsi, sichuan, south China. J. China Univ. Geosci. 19, 496–506. https://doi.org/10.1016/S1002-0705(08)60055-2.
- Liang, D., Guo, T., Bian, L., Chen, J., Zhao, Z., 2009. Some progresses on studies of hydrocarbon generation and accumulation in marine sedimentary regions, southern China (Part 3): controlling factors on the sedimentary facies and development of palaeozoic marine source rocks. Marine Origin Petroleum Geology 14, 1–19. https://doi.org/10.3969/j.issn.1672-9854.2009.02.001 (in Chinese)
- Liao, Z., Hu, W., Cao, J., Wang, X., Hu, Z., 2019. Petrologic and geochemical evidence for the formation of organic-rich siliceous rocks of the Late Permian Dalong Formation, Lower Yangtze region, southern China. Mar. Petrol. Geol. 103, 41–54. https://doi.org/10.1016/j.marpetgeo.2019.02.005.
- Little, S.H., Vance, D., Lyons, T.W., McManus, J., 2015. Controls on trace metal authigenic enrichment in reducing sediments: insights from modern oxygendeficient settings. Am. J. Sci. 315, 77–119. https://doi.org/10.2475/02.2015.01.
- Liu, Q.Y., Li, P., Jin, Z.J., Liang, X.P., Zhu, D.Y., Wu, X.Q., Meng, Q.Q., Liu, J.Y., Fu, Q., Zhao, J.H., 2021a. Preservation of organic matter in shale linked to bacterial sulfate reduction (BSR) and volcanic activity under marine and lacustrine depositional environments. Mar. Petrol. Geol. 127, 104950. https://doi.org/10.1016/j.marpetgeo.2021.104950.
- Liu, S., Yang, Y., Deng, B., Zhong, Y., Wen, L., Sun, W., Li, Z., Jansa, L., Li, J., Song, J., Zhang, X., Peng, H., 2021b. Tectonic evolution of the Sichuan Basin, southwest China. Earth Sci. Rev. 213, 103470. https://doi.org/10.1016/iearscirey.2020.103470
- Liu, W., Yao, J., Tong, J., Qiao, Y., Chen, Y., 2019. Organic matter accumulation on the Dalong Formation (Upper Permian) in western Hubei, South China: constraints from multiple geochemical proxies and pyrite morphology. Palaeogeogr. Palaeoclimatol. Palaeoecol. 514, 677–689. https://doi.org/10.1016/ j.palaeo.2018.11.015.
- Liu, W., Zhang, X., Qiao, Y., Xu, Y., Mou, C., Wu, W., Yao, J., 2022a. Climate-driven paleoceanography change controls on petrology and organic matter accumulation in the upper Permian Dalong Formation, western Hubei Province, southern China. Sediment. Geol. 440, 106259. https://doi.org/10.1016/ i.sedgeo.2022.106259.
- Liu, W., Zhang, X., Qiao, Y., Xu, Y., Mou, C., Wu, W., Yao, J., 2022b. Climate-driven paleoceanography change controls on petrology and organic matter accumulation in the upper Permian Dalong Formation, western Hubei Province, southern China. Sediment. Geol. 440, 106259. https://doi.org/10.1016/j.sedgeo.2022.106259.
- Lu, Y.B., Shen, J., Wang, Y.X., Lu, Y.C., Algeo, T.J., Jiang, S., Yan, D.T., Gou, Q.Y., 2022. Seawater sources of Hg enrichment in Ordovician-Silurian boundary strata, South China. Palaeogeogr. Palaeoclimatol. Palaeoecol. 601, 111156. https://doi.org/10.1016/j.palaeo.2022.111156.
- Liu, Z., Selby, D., 2021. Deep-water osmium-isotope record of the Permian—Triassic interval from Niushan, China reveals potential delayed volcanic signal post the mass extinction. Global Planet. Change 200, 103473. https://doi.org/10.1016/ j.gloplacha.2021.103473.
- Luo, Z., Yong, Z., Liu, S., Zhao, X., Sun, W., 2004. Divergent role of Emei tafrogeny on yangtse palaeoslab and tarim palaeos lab and its significance in geoscience. Xinjing Pet. Geol. 1, 1–7 https://doi.org/10.3969/j.issn.1001-3873.2004.01.001 (in Chinese)
- Matsumoto, H., Coccioni, R., Frontalini, F., Shirai, K., Jovane, L., Trindade, R., Savian, J.F., Tejada, M.L.G., Gardin, S., Kuroda, J., 2021. Long-term Aptian marine osmium isotopic record of Ontong Java Nui activity. Geology 49, 1148–1152. https://doi.org/10.1130/G48863.1.
- McKnight, D.M., Feder, G.L., Stiles, E.A., 1981. Toxicity of volcanic-ash leachate to a blue-green alga. Results of a preliminary bioassay experiment. Environ. Sci. Technol. 15, 362–364. https://doi.org/10.1021/es00085a606.
- McLennan, S., 1993. Weathering and global denudation. J. Geol. 101, 295–303. https://doi.org/10.1086/648222.
- Mclennan, S.M., 2001. Relationships between the trace element composition of sedimentary rocks and upper continental crust. G-cubed 2, 203–236. https://doi.org/10.1029/2000GC000109.
- Meng, Q., Qin, J., Liu, W., Hu, W., Zheng, L., 2008. Experimental study on hydrocarbon generation of multi-cellular benthic macro alga. Acta Pet. Sin. 29, 822–826 https://doi.org/10.3321/j.issn:0253-2697.2008.06.006 (in Chinese).
- Murray, R.W., Leinen, M., 1993. Chemical transport to the seafloor of the equatorial Pacific Ocean across a latitudinal transect at 135°W: tracking sedimentary major, trace, and rare earth element fluxes at the Equator and the Intertropical Convergence Zone. Geochem. Cosmochim. Acta 57, 4141–4163. https://doi.org/10.1016/0016-7037(93)90312-K.
- Muttoni, G., Kent, D.V., Garzanti, E., Brack, P., Abrahamsen, N., Gaetani, M., 2003. Early permian Pangea 'B' to late permian Pangea 'A'. Earth Planet Sci. Lett. 215, 379–394. https://doi.org/10.1016/S0012-821X(03)00452-7.
- Nance, W.B., Taylor, S.R., 1976. Rare earth element patterns and crustal evolution—I. Australian post-Archean sedimentary rocks. Geochem. Cosmochim. Acta 40, 1539—1551. https://doi.org/10.1016/0016-7037(76)90093-4.

Nesbitt, H.W., Young, G.M., 1982. Early Proterozoic climates and plate motions inferred from major element chemistry of lutites. Nature 299, 715–717. https://doi.org/10.1038/299715a0.

- Nichols, G., 2023. Sedimentary and Stratigraphy. Wiley, New York.
- Parker, A.J.G.M., 1970. An index of weathering for silicate rocks. Geol. Mag. 107, 501–504. https://doi.org/10.1017/S0016756800058581.
- Rowe, H.D., Loucks, R.G., Ruppel, S.C., Rimmer, S.M., 2008. Mississippian barnett formation, fort worth basin, Texas: bulk geochemical inferences and Mo–TOC constraints on the severity of hydrographic restriction. Chem. Geol. 257, 16–25. https://doi.org/10.1016/j.chemgeo.2008.08.006.
- Sageman, B.B., Murphy, A.E., Werne, J.P., Ver Straeten, C.A., Hollander, D.J., Lyons, T.W., 2003. A tale of shales: the relative roles of production, decomposition, and dilution in the accumulation of organic-rich strata, Middle—Upper Devonian, Appalachian basin. Chem. Geol. 195, 229–273. https://doi.org/10.1016/S0009-2541(02)00397-2.
- Schoepfer, S.D., Shen, J., Wei, H., Tyson, R.V., Ingall, E., Algeo, T.J., 2015. Total organic carbon, organic phosphorus, and biogenic barium fluxes as proxies for paleomarine productivity. Earth Sci. Rev. 149, 23–52. https://doi.org/10.1016/ i.earscirev.2014.08.017.
- Shan, X.L., Li, J.Y., Chen, S.M., Ran, Q.C., Chen, G.B.A., Liu, C., 2013. Subaquatic volcanic eruptions in continental facies and their influence on high quality source rocks shown by the volcanic rocks of a faulted depression in Northeast China. Sci. China Earth Sci. 56, 1926—1933. https://doi.org/10.1007/s11430-013-4657-7.
- Shen, J., Schoepfer, S.D., Feng, Q.L., Zhou, L., Yu, J.X., Song, H.Y., Wei, H.Y., Algeo, T.J., 2015. Marine productivity changes during the end-Permian crisis and Early Triassic recovery. Earth Sci. Rev. 149, 136–162. https://doi.org/10.1016/ j.earscirev.2014.11.002.
- Song, H.J., Wignall, P.B., Tong, J.N., Song, H.Y., Chen, J., Chu, D.L., Tian, L., Luo, M., Zong, K.Q., Chen, Y.L., Lai, X.L., Zhang, K.X., Wang, H.M., 2015. Integrated Sr isotope variations and global environmental changes through the Late Premian to early Late Triassic. Earth Planet Sci. Lett. 424, 140–147. https://doi.org/10.1016/j.epsl.2015.05.035.
- Sweere, T., van den Boorn, S., Dickson, A.J., Reichart, G.-J., 2016. Definition of new trace-metal proxies for the controls on organic matter enrichment in marine sediments based on Mn, Co, Mo and Cd concentrations. Chem. Geol. 441, 235–245. https://doi.org/10.1016/j.chemgeo.2016.08.028.
- Sykorova, I., Pickel, W., Christanis, K., et al., 2005. Classification of huminite-ICCP system 1994. Int. J. Coal Geol. 62 (1–2), 85–106. https://doi.org/10.1016/j.coal.2004.06.006.
- Sylvestre, G., Evine Laure, N.T., Gus Djibril, K.N., Arlette, D.S., Cyriel, M., Timoléon, N., Jean Paul, N., 2017. A mixed seawater and hydrothermal origin of superior-type banded iron formation (BIF)-hosted Kouambo iron deposit, Palaeoproterozoic Nyong series, Southwestern Cameroon: constraints from petrography and geochemistry. Ore Geol. Rev. 80, 860–875. https://doi.org/10.1016/j.oregeorev.2016.08.021.
- Tribovillard, N., Algeo, T.J., Baudin, F., Riboulleau, A., 2012. Analysis of marine environmental conditions based onmolybdenum—uranium covariation—applications to Mesozoic paleoceanography. Chem. Geol. 324–325, 46–58. https://doi.org/10.1016/j.chemgeo.2011.09.009.
- Tribovillard, N., Algeo, T.J., Lyons, T., Riboulleau, A., 2006. Trace metals as paleoredox and paleoproductivity proxies: an update. Chem. Geol. 232, 12–32. https://doi.org/10.1016/j.chemgeo.2006.02.012.
- Tyson, R.V., Pearson, T.H., 1991. Modern and Ancient Continental Shelf Anoxia: an Overview, vol. 58. Geological Society of London Special Publications, pp. 1–24.
- Vorlicek, T.P., Kahn, M.D., Kasuya, Y., Helz, G.R., 2004. Capture of molybdenum in pyrite-forming sediments: role of ligand-induced reduction by polysulfides 1 1Associate editor: M. Goldhaber. Geochem. Cosmochim. Acta 68, 547–556. https://doi.org/10.1016/S0016-7037(03)00444-7.
- Wang, H., 1988. A sedimentary model for interfingering clear-water and turbid water deposists. J. Palaeogeogr. 6, 32–37.
- Wang, Y., Cao, J., Zhang, B., Hu, G., Liu, J., Zhang, B., Liao, Z., Xiao, D., 2023. Effects of emeishan large igneous province on organic matter accumulation, Sichuan Basin, China. Palaeogeogr. Palaeoclimatol. Palaeoecol. 632, 111862. https:// doi.org/10.1016/j.palaeo.2023.111862.
- Wang, Z., Tan, J., Boyle, R., Hilton, J., Ma, Z., Wang, W., Lyu, Q., Kang, X., Luo, W., 2020. Evaluating episodic hydrothermal activity in South China during the early Cambrian: implications for biotic evolution. Mar. Petrol. Geol. 117, 104355. https://doi.org/10.1016/j.marpetgeo.2020.104355.
- Wignall, P.B., 2001. Large igneous provinces and mass extinctions. Earth Sci. Rev. 53, 1–33. https://doi.org/10.1016/S0012-8252(00)00037-4.
- Wignall, P.B., Twitchett, R.J., 1996. Oceanic anoxia and the end Permian mass extinction. Science 272, 1155–1158. https://doi.org/10.1126/science.272.5265.1155.
- Wu, C., Zhang, L., Zhang, T., Tuo, J., Song, D., Liu, Y., Zhang, M., Xing, L., 2020. Reconstruction of paleoceanic redox conditions of the lower Cambrian Niutitang shales in northern Guizhou, Upper Yangtze region. Palaeogeogr. Palaeoclimatol. Palaeoecol. 538, 109457. https://doi.org/10.1016/j.palaeo.2019.109457.
- Wu, W., Liu, W., Mou, C., Liu, H., Qiao, Y., Pan, J., Ning, S., Zhang, X., Yao, J., Liu, J., 2021. Organic-rich siliceous rocks in the upper Permian Dalong Formation (NW middle Yangtze): provenance, paleoclimate and paleoenvironment. Mar. Petrol. Geol. 123, 104728. https://doi.org/10.1016/j.marpetgeo.2020.104728.
- Wu, Z., He, S., He, Z., Li, X., Zhai, G., Huang, Z., 2022. Petrographical and geochemical characterization of the Upper Permian Longtan formation and Dalong Formation in the Lower Yangtze region, South China: implications for provenance, paleoclimate, paleoenvironment and organic matter accumulation

- mechanisms. Mar. Petrol. Geol. 139, 105580. https://doi.org/10.1016/j.marpetgeo.2022.105580.
- Xia, G.D., Ye, Y.H., Liu, S.G., Wang, H., Song, J.M., Sun, W., Ran, B., Jiao, K., Xie, G.L., Deng, B., Li, Z.W., Zeng, Y., 2024. Paleoenvironmental evolution and organic matter accumulation of the lower Cambrian Maidiping marine black shales in the intracratonic basin, western margin of Sichuan Basin, South China. Int. Geol. Rev. 66, 2249–2268. https://doi.org/10.1080/00206814.2023.2278054.
- Xiao, B., Liu, S.G., Ran, B., Li, Z.W., 2019. Geochemistry and sedimentology of the Upper Ordovician—lower Silurian black shale in the northern margin of the Upper Yangtze Platform, South China: implications for depositional controls on organic-matter accumulation. Aust. J. Earth Sci. 67, 129–150. https://doi.org/ 10.1080/08120099.2019.1626765.
- Yan, D., Li, S., Fu, H., Jasper, D.M., Zhou, S., Yang, X., Zhang, B., Mangi, H.N., 2021. Mineralogy and geochemistry of lower silurian black shales from the Yangtze platform, south China. Int. J. Coal Geol. 237, 103706. https://doi.org/10.1016/ i.coal.2021.103706.
- Yan, D., Wang, H., Fu, Q., Chen, Z., He, J., Gao, Z., 2015. Geochemical characteristics in the Longmaxi Formation (early silurian) of South China: implications for organic matter accumulation. Mar. Petrol. Geol. 65, 290—301. https://doi.org/ 10.1016/j.marpetgeo.2015.04.016.

- Yang, S.C., Hu, W.X., Fan, J.X., Deng, Y.Y., 2022. New geochemical identification fingerprints of volcanism during the Ordovician-Silurian transition and its implications for biological and environmental evolution. Earth Sci. Rev. 228, 104016. https://doi.org/10.1016/j.earscirev.2022.104016.
- Yu, Y., Li, P., Guo, R., Zhao, Y., Li, S., Zou, H., 2021. Upwelling-induced organic matter enrichment of the upper permian Dalong Formation in the Sichuan Basin, SW China and its paleoenvironmental implications. Palaeogeogr. Palaeoclimatol. Palaeoecol. 576, 110510. https://doi.org/10.1016/j.palaeo.2021.110510.
- Zhang, B., Yao, S., Wignall, P.B., Hu, W., Ding, H., Liu, B., Ren, Y., 2018. Widespread coastal upwelling along the eastern paleo-tethys margin (south China) during the middle permian (guadalupian): implications for organic matter accumulation. Mar. Petrol. Geol. 97, 113–126. https://doi.org/10.1016/j.marpetgeo.2018.06.025.
- Zheng, B., Mou, C., Wang, Y., 2024. Organic matter accumulation in response to tectonism: new data from the Upper Permian Dalong Formation black shales in the Western Hubei Basin, South China and its implications for the end-Permian mass extinction. Sediment. Geol. 464, 106621. https://doi.org/10.1016/ j.sedgeo.2024.106621.